Advances in solid state photon detectors

PUBLISHED BY IOP PUBLISHING FOR SISSA

RECEIVED: *December 17, 2008*
ACCEPTED: *February 24, 2009*
PUBLISHED: *April 7, 2009*

REVIEW

Advances in solid state photon detectors

D. Renker[a,1] **and E. Lorenz**[b,c]

[a] *Paul Scherrer Institute, Villigen, Switzerland*
[b] *Max Planck Institute for Physics, Munich, Germany*
[c] *Eidg. Technische Hochschule, Zurich, Switzerland*

E-mail: dieter.renker@psi.ch

ABSTRACT: Semiconductor photodiodes were developed in the early 'Forties approximately at the time when the photomultiplier tube became a commercial product (RCA 1939). Only in recent years, with the invention of the Geiger-mode avalanche photodiodes, have the semiconductor photo detectors reached sensitivity comparable to that of photomultiplier tubes. The evolution started in the 'Sixties with the p-i-n (PIN) photodiode, a very successful device, which is still used in many detectors for high energy physics and a large number of other applications like radiation detection and medical imaging. The next step was the development of the avalanche photodiode (APD) leading to a substantial reduction of noise but not yet achieving single photon response.

The weakest light flashes that can be detected by the PIN diode need to contain several hundreds of photons. An improvement of the sensitivity by 2 orders of magnitude was achieved by the development of the avalanche photodiode, a device with internal gain. At the end of the millennium, the semiconductor detectors evolved with the Geiger-mode avalanche photodiode into highly sensitive devices, which have an internal gain comparable to the gain of photomultiplier tubes and a response to single photons. A review of the semiconductor photo detector design and development, the properties and problems, some applications and a speculative outlook on the future evolution will be presented.

KEYWORDS: Photon detectors for UV, visible and IR photons (solid-state) (PIN diodes, APDs, Si-PMTs, CCDs, EBCCDs etc); Photon detectors for UV, visible and IR photons (solid-state)

[1] Corresponding author.

doi:10.1088/1748-0221/4/04/P04004

Contents

2009 JINST 4 P04004

2009 JINST 4 P04004

1 Introduction

1.1 Early detection of light by semiconductor detectors

The p-n junction in silicon was discovered at the Bell Telephone Labs by Russel Ohl in 1940 when he observed the photovoltaic effect when light was flashed onto a silicon rod [1].

In the late 1930s, Ohl had investigated the use of silicon crystals as rectifiers in radar detectors. He found that with higher quality crystals their finicky behaviour went away - but so did their ability to operate as a radio detector. At the beginning of 1940 he found that one of his purest crystals nevertheless worked well and, interestingly, it had a clearly visible crack near the middle. A surprising effect was that the current flowing through the silicon rod jumped appreciably when exposed to bright light. Ohl also noticed that different parts of the crystal yielded opposite electrical effects when tested with a "cat's whisker" style probe, a thin metal wire touching against the semiconductor crystal as was used in early radios (patented by Ferdinand Braun in 1899). He invited several other people to see this crystal and Walter Brattain immediately realized there was some sort of junction at the crack. It was found that the crack had developed because either side contained different impurities. One side of the crystal had impurities (so-called donors), in this case phosphor, that added extra electrons, the other side had impurities (so-called acceptors), boron, that wanted to bind to these electrons. They called the two regions n-type (for negative) and p-type (positive). Because the two parts of the crystal were in contact with each other, the electrons could be pushed out of the side, which had extra electrons and replaced by new ones being provided (from a battery, for instance) where they would flow to the other side and be collected by the whisker filament. However, when the voltage was reversed, the electrons being pushed into the collector would quickly fill up the "holes" (the electron-needy impurities) and conduction would stop almost instantly. The

p-n junction in the middle of the crystal created a solid-state diode. Light striking this junction stimulated electrons to flow from the n-side to the p-side, resulting in an electric current.

A vigorous effort began in order to learn how to build the new diodes on demand. Within a year germanium (Ge) production had been perfected to the point where military-grade diodes were being used in most radar sets.

The development of the germanium diodes and later of transistors opened the door to countless applications of solid state electronics. From 1950 through to the early 1970s, this area provided an increasing market for germanium but then high purity silicon (Si) began replacing germanium in transistors, diodes, and rectifiers. Silicon has superior electrical properties but requires much higher purity samples - a purity, which could not be commercially achieved in the early days.

The semiconductor material used to make a photodiode must have properties matched to the energy of the photons to be detected, because only photons with sufficient energy to excite electrons across the material's bandgap will produce significant photocurrents. Because of the greater bandgap (1.12 eV for Si and 0.67 eV for Ge), silicon-based photodiodes generate less noise than germanium-based photodiodes. Nevertheless, germanium photodiodes must be used for wavelengths longer than approximately 1 μm (or other semiconductor materials like indium gallium arsenide). Gallium arsenide (GaAs) with a bandgap of 1.4 eV would be even more advantageous for low noise photodiodes but it has deep level defects (EL2) and it lacks one of the most important properties of Si, which is the easy formation of a top layer passivation by silicon dioxide - one of the best insulators with excellent transmission of light even in the UV range. Silicon dioxide can easily be formed onto silicon circuits, and such layers adhere well to the underlying Si. GaAs does not form a stable adherent insulating layer.

Silicon photodiodes are sensitive in the wavelength range of some 150 to 1100 nm, thus covering well the emission wavelength of almost all organic and inorganic scintillators and of Cherenkov radiators used in particle physics, medical imaging and radiation detection.

1.2 Structure of this article

This article will concentrate on the status of novel silicon photon detectors with high internal gain to detect single photons, the so-called Geiger mode avalanche photodiodes (G-APD). Nevertheless, for the sake of clarity, it will at first elaborate on the initial developments of semiconductor photon detectors, e.g. from PIN photodiodes without internal gain and rather high noise levels to Avalanche photodiodes (APD) operating below breakdown voltage in the linear mode with modest gain and on the first approaches to detect single photons to finally to the development of the G-APDs as true single photon detectors. The article will concentrate on developments of photon detectors for research where there exist a strong demand on very low level, fast photon detection and will only touch consumer applications very briefly. To highlight the developments we quote state of the art photon detection efficiencies of the 3 classes of photodetectors:

Photodetector type	**Minimal detectable signal**	**Bandwidth**
Silicon PIN photodiodes	200-300 photoelectrons	few 100 kHz
Silicon APD	10-20 photoelectrons	Mhz- few100 Mhz
Silicon G-APD	1 photoelectron	Mhz-few 100 Mhz

2009 JINST 4 P04004

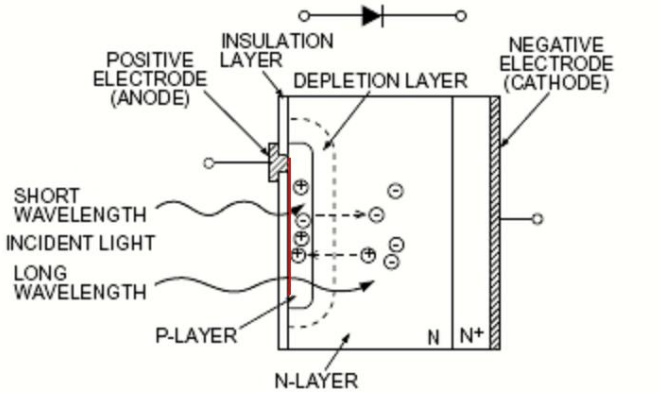

Figure 1. View of a standard photodiode. The red line indicates the very thin p++ layer.

The article has the following structure. In section 2, the fundamentals of the photon detection in silicon photodiodes will be discussed followed by practical designs in sections 3, 4 and 5. In section 6, the amplification processes in linear mode APDs will be described. Section 6, the main part of the paper, covers the novel G-APDs. Finally, the article concludes with a brief summary of some applications and an outlook for the future as well as a list of possible improvements in the next years.

2 Detection of photons with silicon photodiodes

Figure 1 shows an isometric, simplified view of a standard photodiode with a p-n structure, top layer passivation by SiO_2 and the contacts. Photons impinging onto the diode can undergo one of the following processes

- Surface reflectivity losses
- Absorption losses in the top protection layer
- Conversion inside the top high conductive p++ layer with rapid recombination, mostly for UV light
- Conversion in the top p-layer (assumed to be depleted), mostly in the case of short wavelengths
- Conversion in the depleted n-layer, mostly in the case of longer wavelengths
- Conversion in the undepleted n-layer, mostly for IR light
- No absorption at all, mostly in the case of long wavelength IR light

In the following we will discuss the processes in more detail.

2009 JINST 4 P04004

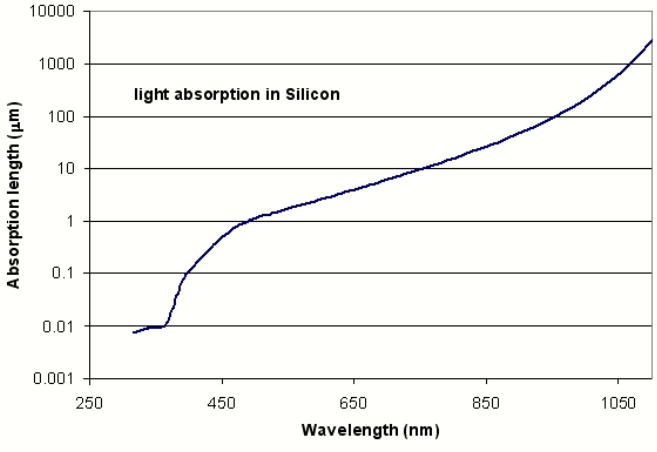

Figure 2. The photon absorption length in μm of silicon versus wavelength [3].

2.1 Light reflection at the surface

When light from a low refractive index medium, for example air, impinges on a high refractive index surface, such as silicon with n $\approx$ 3.5, quite a large fraction of photons is reflected. Usually a silicon photodiode is covered with a thin layer of silicon oxide (n = 1.46), which also has considerable influence on the reflection of photons at the surface, specifically on the interface between the silicon oxide and the silicon. Depending on the wavelength and the oxide thickness, 20 to 30 percent of the incident light can be lost because of this reflection (dependent on the passivation material and its thickness resulting in possible interference effects). This causes a serious decrease in the quantum efficiency (QE) of the photodiode. Fortunately, reflection losses can be significantly reduced using anti-reflecting coatings. With a suitable coating made of several thin layers with different refraction indices, the reflection losses can be reduced to values below 10 percent over the entire visible spectrum [2].

2.2 Photon absorption losses in the passivation layer

Most passivation layers are of very high optical quality and losses can be neglected, except in the UV region where nearly all materials eventually show strong absorption at very short wavelengths below $\sim$300 nm.

2.3 Photon absorption in silicon

Photons that have passed the oxide layer and have entered the silicon bulk will be almost entirely absorbed. The absorption length, the inverse of the absorption coefficient α, depends strongly on the wavelength of the incident light, as can be seen in figure 2.

The photon flux at a distance d from the surface I(d) is given by:

$$\mathrm{I(d)} = \mathrm{I(0)exp}(-\alpha \mathrm{d}) \tag{2.1}$$

where I(0) is the incident flux entering the silicon.

2009 JINST 4 P04004

At energies below the bandgap of 1.12 eV, photons can only be absorbed by free electrons and the absorption coefficient is very small. At energies above 1.12 eV, photons are absorbed by 'lifting' electrons from the valence band to the conduction band. In this process a phonon is needed for momentum conservation because silicon has an indirect bandgap structure. The absorption of a photon with energies close to the bandgap requires a phonon with high momentum. Their occurrence is small and consequently the absorption probability is small. With increasing photon energy, less momentum of the phonons is required, more phonons are available and in turn the absorption coefficient increases. Above 3.4 eV (wavelength ∼350 nm) a direct transition is possible and causes a further increase of the absorption coefficient.

The top layer of a photodiode has normally a high concentration of implanted dopants to ensure a small series resistance and a uniform response. This p++ (or n++) layer cannot be depleted and the electrons and holes created by a photon absorption in this layer have a very short life time, i.e. they either recombine promptly or have to move by diffusion and can recombine at interface states at the surface. The sensitivity of photodiodes for photons with very short wavelength, i.e. of very short absorption length, is strongly reduced by this effect. On the other hand, photons of a very long wavelength have a small absorption coefficient and therefore may penetrate the entire photodiode without being absorbed and detected.

2.4 Charge collection

The photon absorption process generates in the semiconductor electron-hole pairs, which, depending on the purity of the material, can have quite a long lifetime of up to msec in high purity silicon. Depending on the local electrical field strength and impurity concentration the free charge carriers can either:

- Move by diffusion in the field-free regions
- Move under the influence of the electrical field and can be separated due to the two signs of their charge. This movement overlaps with diffusion and can either be stronger or weaker than diffusion displacement, depending on the field strength.
- Recombine very quickly (as already mentioned) in the high impurity zones

2.4.1 Diffusion

Once a photon has generated an electron-hole pair in the silicon structure, the electron travels to the p-n junction even without an applied external electric field. Electron travel in the absorption layer is governed by diffusion according to Fick's first law:

$$\Gamma_e = -D_e \frac{dn}{dz} \tag{2.2}$$

where Γ_e is the net electron flux, D_e is the electron diffusion coefficient, z is the position of the electron and dn/dz is the photoelectron concentration gradient. The diffusion coefficient is related to the mobility of the electrons in the silicon layer by the Einstein relationship, which is generalized for carriers away from the band edges.

$$D = \left(\frac{kT}{q}\right) \cdot \mu_e \tag{2.3}$$

2009 JINST 4 P04004

where k is the Boltzmann constant, T the temperature in Kelvin, q the electric charge and μ_e the mobility. The mobility decreases for increased substrate doping concentration. For holes, the diffusion equation is very similar except that the hole mobility is much smaller than that of electrons.

A diode is formed by the combination of a layer of p-type material (typically doped with an element of the IIIrd group, for example boron in silicon) and a layer of n-type material (usually doped with an element of the Vth group in the periodic system such as phosphor or arsenic). Free electrons from the n-type side of the junction diffuse to combine with holes on the p-type side and vice-versa. This diffusion creates an area devoid of mobile charge carriers (the so-called depletion region) on both sides of the metallurgical junction. The depletion region extends into both n (to a distance x_n) and p (to a distance x_p) sides of the junction according to:

$$N_A x_p = N_D x_n \tag{2.4}$$

where N_A is the concentration in cm^{-3} of the p-type dopant and N_D is the concentration of n-type dopant. Charge neutrality is preserved such that any increase of the dopant concentration on one side of the junction is met with a corresponding increase in depletion region width on the other side of the junction.

A feature of the p-n junction is the built-in (or internal) electric field. When a net diffusion of electrons from the n-region to the p-region and of holes from the p-region to the n-region takes place, a space charge due to the donor and acceptor ions is formed. Thus, after a certain number of electrons and holes have flown from one region to the other, an electric field is built up, preventing a further flow of the carriers. The maximal electric field E_{max} can be accurately calculated by:

$$|E_{\max}| = \frac{q \cdot N_A \cdot x_p}{\varepsilon_S} \tag{2.5}$$

where q is the electron charge, N_A is the substrate doping concentration, x_p is the extension of the depletion region and ε_s is the permittivity of silicon. The total potential from one side of the junction to the other is given by:

$$\Phi_T = \frac{1}{2} E_{\max} \cdot W = \frac{1}{2} E_{\max} \cdot (x_n + x_p) \tag{2.6}$$

The width W of the depleted region of a step junction can, on the other hand, be obtained from the total electrostatic potential:

$$W = \sqrt{\frac{2K_S\varepsilon_0}{q} \cdot \frac{N_A + N_D}{N_A \cdot N_D} \cdot \Phi_T} \tag{2.7}$$

K_s is the dielectric constant of Si and ε_0 the permittivity of the vacuum.

By applying a reverse bias to the diode, the total electrostatic potential across the junction will increase by that amount of voltage. As a result, the width of the space charge region on both the n-side and on the p-side will increase with the sqrt(Φ_T).

2.4.2 Drift of electrons and holes in an externally applied electric field

Carriers in a semiconductor undergo a continual thermal motion interrupted by collisions. If an electric field is applied a velocity component is superimposed upon the thermal motion of the

2009 JINST 4 P04004

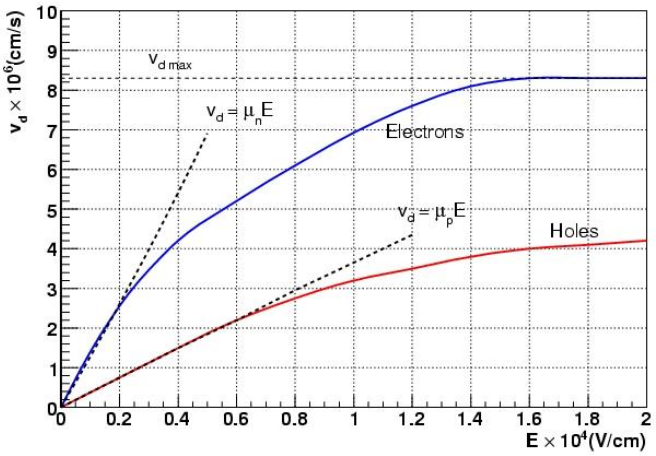

Figure 3. Effect of an electric field on the drift velocities of carriers in silicon [4].

carriers. The magnitude of the acceleration A after a collision is given by Newton's law:

$$A = q \cdot E/m \tag{2.8}$$

where m is the effective mass of the electrons replacing the mass of a free electron. It essentially corrects for the effect of the presence of the semiconductor crystal lattice on the behavior of the electrons. In the time interval between collisions t_{coll} the average drift velocity is

$$\vec{v}_{drift} = \frac{qE}{2m} t_{coll} = \mu_e \cdot E \tag{2.9}$$

As the drift velocity becomes comparable to the thermal velocity, its dependence on the electric field departs from the simple relationship given above. This is illustrated by the experimental measurements of the drift velocity of electrons and holes in silicon as a function of the electric field, shown in figure 3. It can also be seen that the mobility of electrons is larger than the mobility of holes. The time interval between collisions is determined by the various mechanisms by which the electrons or holes can lose their acquired drift velocity. The probability of a collision taking place in time unit, $1/t_{coll}$, is the sum of the probabilities of collisions due to such scattering mechanisms:

$$\frac{1}{t_{coll}} = \frac{1}{t_{coll,impurity}} + \frac{1}{t_{coll,lattice}} \tag{2.10}$$

with the 2 terms corresponding to the two most important scattering mechanisms, impurity and lattice scattering. At high temperatures (room temperature and higher), lattice scattering dominates and the impurity concentration has little effect on the mobility. At a certain high field strength, the movement of electrons and holes not longer follows the process described above but the interaction of the charge carriers can lead to impact ionization, i.e. to the generation of additional e-h pairs. The number of charge carriers is then no longer identical to the number of absorbed photons but can reach quite high numbers, i.e. an internal 'amplification' can occur. Before discussing this effect and photon detectors with internal gain, we want to present briefly some standard types of photon detectors without internal gain.

2009 JINST 4 P04004

3 Photon detectors without internal amplification

3.1 Integrating detectors

Integrating detectors are slow where the signal is proportional to the number of photons per time interval. Integrating light detectors seldom have sufficient sensitivity in the low photon level and are nowadays mostly found in image processing for consumer or medical applications. Best known are simple versions, called Charged Coupled Devices (CCD), which can be found in digital cameras as well as in highly sophisticated devices in astronomical telescopes or as X-ray detectors on board of satellites. CCDs made of an array of pixels have a quantum efficiency of 70% and more over quite a wide spectral range, making them far more sensitive than photographic films, which capture only about 2% of the incident light.

Faster, cheaper and less power-consuming are the Monolithic Active Pixel Sensors (MAPS) or Complementary Metal Oxide (CMOS) image sensors, which, in contrast to CCDs, are compatible with the Complementary Metal Oxide production technology. All components necessary for the readout can be implanted on the same single piece of silicon.

In hybrid pixel detectors, a pixelized sensor chip made of any kind of semiconductor material is bump-bonded to a readout chip. This type of sensor is installed in all Large Hadron Collider (LHC) detectors, in ALICE, ATLAS, CMS and LHCb (in the RICH system) for a precise measurement of particle tracks. Photon detection with this technique is only possible when the photon energy exceeds several keV. In imaging applications, the hybrid pixel detectors accumulate the incident radiation through the counting of the radiation quanta in every pixel. The analog part of the pixel electronic is almost identical to the one for LHC pixel detectors while the periphery has been replaced by counting circuits [5].

For radiography the MEDIPIX (versions 1, 2 and 3) chip [6] and the MPEC chip [7] have been developed. These chips can be combined with sensors made of various semiconductor materials including the high-Z material CdTe.

The first large-scale hybrid pixel detector in operation is the PILATUS detector [8] developed at the Paul-Scherrer-Institute in Switzerland for proton crystallography experiments such like at the Swiss Light Source (SLS). A remarkable low energy threshold below 3 keV has been obtained with 320 μm thick Si sensors [9]. PILATUS is a modular system. Each module consists of a Si sensor bump-bonded to an array of 8×2 chips using indium balls. It has 487×195 pixels with a pixel size of 0.172 mm. The 16 chips of a module are read out in parallel within a read-out time of $\sim$2 ms. The PILATUS 6M contains 6×12 modules, spans an area of 424×435 mm^2 and has in total 6 million pixels.

In particle physics, astrophysics and nuclear medical imaging, the arrival time of a photon or flashes of photons coming from a scintillator or a Cherenkov radiator is very important for the event reconstruction and/or for background suppression.

The amplitude of the signals needs to be analyzed event by event in order to get information about the energy of the primary particle that caused the light flash.

3.2 PIN photodiode

The PIN photodiode is one of the simplest types of photodiodes. It is an intrinsic piece of high-ohmic semiconductor sandwiched between two heavily doped n+ and p+ regions (figure 4) It is

2009 JINST 4 P04004

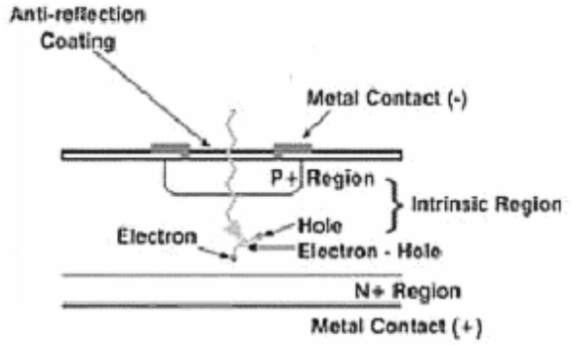

Figure 4. Structure of a PIN photodiode.

produced by standard semiconductor processes: boron diffusion on one side and phosphor diffusion on the other side of a high purity n-type silicon wafer. This configuration produces a field, which, even without an external field supplied, will tend to separate charges produced in the depleted region. The separated charges will be swept to the terminals and detected as current provided that they do not already recombine inside the semiconductor. The thick layer of intrinsic silicon (300 μm) reduces the capacitance of the diode and, through this, the serial noise and makes it sensitive to red and infrared light, which has a rather long absorption length in silicon (section 2.2). Since this layer has a very low concentration of dopants, only a small voltage is required to deplete the device completely. An added advantage is that the recombination/generation time constant is the longest one in case of undoped materials, which also provide a minimal thermal generation current. Clearly the top p-layer, which cannot be depleted, needs to be transparent to incoming light. A thin, but highly doped layer is used in silicon photodiodes.

For an easy coupling of the PIN diode to a light source, for example to a scintillating crystal, the surface is usually covered by a thin layer of highly transparent resin that protects the bond wire as well as preventing contamination and possible mechanical damage of the very thin p++ (n++) layer and silicon bulk. Extensive studies resulted in a stable resin, which has very little water absorption, is free of hydrolysable chlorides and sodium and has only little effect on the loss of quantum efficiency [10]. Normally, these protective layers have a transmission cutoff around 320-290 nm.

PIN photodiodes were the first large scale application of silicon sensors for low light level detection (defined here as a signal of a few hundred photons per unit area within less than a few μsec) in research. Their development was driven to find a replacement for photomultipliers in high energy physics (HEP) experiments, where detector elements had to be placed in magnetic fields or in the magnet fringe fields and was often dictated by the needs for a very compact light sensor or one that did not need high operation voltages.

Basically, general-purpose detectors in high energy physics experiments need magnetic fields for the measurement of the momentum of charged particles as well as photon detectors for other purposes such as, for example, scintillation calorimeters for hadrons and/or electromagnetic particle detection/measurements. These detectors often have to be placed inside magnetic fields or in stray fields. Photomultiplier tubes are already affected by very weak magnetic fields and therefore have to be either heavily shielded or replaced by solid-state devices. For high light yield scintillator

2009 JINST 4 P04004

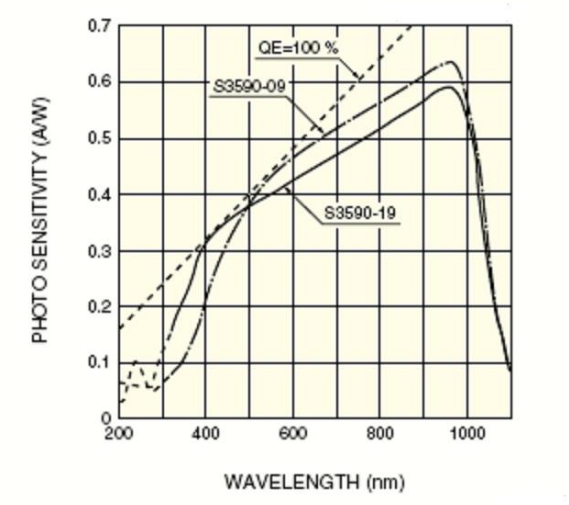

Figure 5. Spectral sensitivity of some commercial PIN diodes as a function of the wavelength. The dashed line indicates a quantum efficiency of 100%. (Hamamatsu S3590-18 [18]).

calorimeters, the PIN photodiode was considered as a possible replacement candidate. In the early 'Eighties, silicon photodiodes were still produced by the diffusion implantation technique resulting in large leakage current and in turn too noisy devices. The breakthrough came by the replacement of the diffusion technique by ion implantation allowing the leakage currents to be reduced by a factor > 1000 (from many μA leakage current/cm^2 to below 1 nA/cm^2 leakage currents) and to enhance very much the 'blue' sensitivity by a very shallow p++ front layer. Initial prototype studies of the photodiode readout for gamma-ray detectors based on scintillating crystals can be found [e.g. 11]. The L3 and CLEO II collaborations were the first to propose the use of PIN photodiodes for the readout of a large BGO [12] and, as well as, for a CsI(Tl) [13] calorimeter for gamma detection and electron identification. Nowadays, most large scintillation gamma calorimeters use PIN photodiodes as readout elements. (CLEO [13], L3 [12], Crystal Barrel [14], BELLE [15], BABAR [16], GLAST [17] ...).

A calorimeter made of CsI(Tl) crystals and a PIN photodiode readout was first built at the MPI Munich [11] and on a large scale by the CLEO collaboration [13]. CsI(Tl) has a photon yield, which is even higher than that of NaI(Tl) but the emission wavelength peaks at 550 nm. Photodiodes have at this wavelength a quantum efficiency (QE) of $\sim$80% (figure 5) while photomultiplier tubes (PMT) have at most only about 10-15 % QE. The detectors at the B-factories BELLE [15] and BABAR [16] have the same type of calorimeter and all achieve an energy resolution better than 2% for photons with an energy of 1 GeV. Limitations in the resolution were dominated by non-uniform light collection and leakage of some shower particles out of the calorimeter. Another source of some fluctuations were charged particles passing the depleted layer of the PIN diodes, thus creating rare but large fake signals by ionization. This so-called nuclear counter effect will be treated in one of the next sections.

The operation of a PIN photodiode is simple and reliable, but, since it has no internal gain, a charge sensitive amplifier and a low bandwidth filter amplifier are needed for the detection of low light level signals above the sizeable noise caused by the leakage current and the large diode

2009 JINST 4 P04004

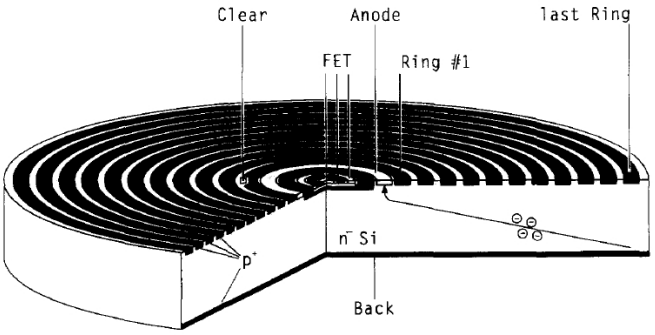

Figure 6. Cross section of a cylindrical silicon drift detector with an integrated n-channel JFET. The entrance window is the non-structured backside. Reprinted from [20].

capacitance, which is typically some 40 pF/cm^2. On the other hand due to the absence of internal gain, PIN photodiodes offer an exceptional stability. For the treatment of noise, we refer to [19]. The use of a charge-sensitive preamplifier and a filter amplifier makes the signal slow. The smallest light flash to be detectable above noise needs to be several hundred photons for state of the art cm^2 PIN photodiodes and filter time constants above a few μsec.

PIN diodes with areas of 10 cm^2 and more are nowadays available and it is easy to fabricate position sensitive devices arrays — even monolithic ones — with a large number of elements. As mentioned, the noise of large PIN photodiodes increases proportionally to the area, respectively to the diode capacitance. If a low noise for a large area readout is required, a possible way out is to drift the photoelectrons to a small collection area with a low capacitance. A caveat is that the drift collection times can be quite long and again the readout will be rather slow.

The next section will briefly cover such photodiodes.

3.3 Silicon drift photodiode

The silicon drift photon detector (SDD) is a fully depleted diode, in which an electric field nearly parallel to the surface is created by properly biased continuous field strips. Figure 6 shows a typical example. The field configuration drives free electrons created anywhere in the depleted volume towards a collecting anode in the center (figure 6). The unique feature is a low noise due to an extremely low anode capacitance, which is, moreover, independent of the detector area. It is possible to achieve a noise level of only a few electrons, albeit with a jitter in time due to the normally unknown photon conversion location and thus to the drift delay. To take full advantage of the low output capacitance, the front-end n-channel JFET of an amplifier can be integrated on the detector chip close to the n$^+$ implanted anode.

3.3.1 Examples reflecting the improved performance

With a monolithic array of 6 SDDs with 3.5 mm^2 diameter and 300 μm thickness each, an energy resolution of 225 eV full width half maximum (FWHM) for the Mn$_{K\alpha}$ line from a ^{55}Fe source has been achieved at room temperature when gammas converted directly inside the silicon (the Equivalent Noise Charge (ENC) contribution of the electronics alone was ENC = 22 e) and 145 eV FWHM at -50 °C (ENC = 9.6 e) [20].

2009 JINST 4 P04004

Another example is given in [21, 22]. A circular SDD with an active area of 30 mm^2 has been coupled to the high light yield scintillator $LaBr_3(Ce)$ and yielded an energy resolution of 2.7% FWHM for the 662 keV line of ^{137}Cs when converted in the scintillator.

3.4 Special PIN photodiode features related to their use in particle research experiments

The replacement of PMTs by PIN photodiodes for many low level light applications began in the mid-1980s. Many optimization developments were carried out in the following years and the results helped to improve the diodes. There exists now a vast amount of reports dealing with these improvements, such as optimization of the QE, large area diodes, low capacitance, low leakage current etc. As the PIN photodiode is now a mature device produced by many companies, we will not discuss these items in more detail but refer the reader to the many publications now available. Only two specific features related to the application in particle detectors will be briefly mentioned: the so-called nuclear counter effect and the problem of radiation damage.

3.4.1 Nuclear counter effect

The full active thickness of the PIN photodiodes and the SDDs (typically) is also sensitive to X-rays as well as to traversing charged particles. For example, in calorimetric applications charged particles (e.g. e^+ and e^-), which leak out at the rear end of the scintillating crystals, pass the diode and produce an unwanted addition to the signal, the so-called nuclear counter effect. A minimum ionizing particle (MIP) creates about 100 electron-hole pairs per micrometer in silicon. This makes in a 300 μm depletion layer 30.000 electron-hole pairs, which fake at least 2 MeV additional energy in a CsI(Tl) calorimeter and much more when a less efficient scintillator like $PbWO_4$is used.

3.4.2 Radiation hardness

Silicon photodiodes suffer from radiation in 2 ways [23]:

- Ionizing radiation (X-rays, γ-rays, charged particles) can deteriorate the Si-SiO_2 interface. Stationary charges are built up, which can reduce the quantum efficiency and increase the surface currents and, in turn, the noise.

- Neutrons and charged particles cause in the bulk silicon defects, which act as generation/recombination centers and increase the bulk dark current. The electron in transition between bands passes through a state created in the band gap by an impurity or defect in the lattice. This state can absorb differences in momentum between the carriers; therefore. this process is the dominant generation and recombination process in silicon and other indirect bandgap materials. The energy is exchanged in the form of lattice vibration, e.g. a phonon exchanging thermal energy with the material (Shockley-Read-Hall process). The defects, in addition, behave like positive dopants and increase the resistivity of the silicon. At high particle fluences the depletion region will be reduced, which, when not compensated by higher bias voltages, will decrease the collection efficiency.

The dominant damage effect in detectors for particle physics is the bulk damage due to the displacement of lattice atoms. It is quantified and normalized for various particle types at different energies

2009 JINST 4 P04004

using the non-ionizing energy loss (NIEL) scaling hypothesis [24]. The displacement damage of 1 MeV neutrons is used as a normalizing value.

The creation of defects, which is responsible for the increase of the dark current, is a volume effect, therefore usually the increase in the dark current I_d can be expressed by

$$I_d = \alpha \cdot V \cdot \Phi \tag{3.1}$$

where V is the volume of the detector and Φ is the fluence. The parameter α has been measured by different groups, see for instance [25], and its value is

$$\alpha = (8-10) \cdot 10^{-17} \mathrm{A/cm} \tag{3.2}$$

for 1 MeV neutrons at 18°C and when measured 2-3 days after the irradiation.

4 The (silicon) Avalanche Photodiode (APD)

The APD is another step towards increasing the sensitivity of photon detectors by reducing the noise at high bandwidth. An avalanche photodiode (APD) is a p-n device with internal gain due to the high internal field at the junction of positive and negative doped silicon. In an APD, a photoelectron in this field gains enough energy to create an electron-hole pair by impact ionization; both the initial electron and the additional electron again undergo high acceleration and can initiate further electron-hole pairs — thus starting an avalanche. If the electrical field is not too high, the accelerated holes do not gain enough energy to create e-h pairs in addition, or else the process runs out of control and a breakdown can occur. The multiplication in practical APDs is moderate, between 50 and 200. A gain of 10^4 is in principle possible but at values higher than a few hundred, the environment (e.g. temperature and voltage supply) needs to be highly regulated because the APD has to be operated extremely close to the breakdown voltage.

There are many theories describing impact ionization. Each theory attempts to provide a single characteristic model for all devices. It was concluded by McIntyre [26] that a characteristic intrinsic ionization coefficient does not exist for all devices and that any measured value is a weighted average, which is characteristic only of the photodiode structure for which it was measured. Regardless of the model, it is generally accepted that the electric field must reach a critical value, called the impact ionization threshold, which is approximately $1.75 \cdot 10^5$ V/cm for silicon, before electrons can gain sufficient kinetic energy to generate electron/hole pairs [26]. The field strength for holes to generate impact ionization is around $2.5 \cdot 10^5$ V/cm [27]. The impact ionization process generates M additional carriers on average, where M is called the multiplication gain.

4.1 Structure of common APDs

Commonly 3 alternative APD structures are used:

- beveled edge,
- reach-through,
- reverse or buried junction APD.

2009 JINST 4 P04004

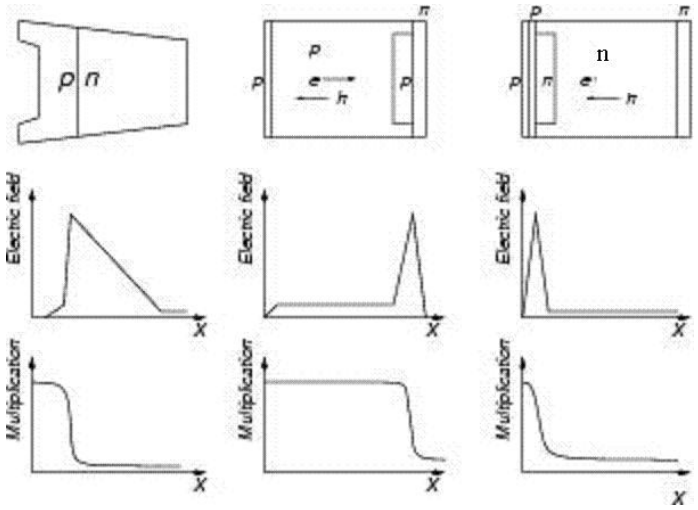

Figure 7. Device structures, electric field profiles and electron/hole multiplication for (left) beveled-edge, (center) reach-through and (right) shallow junction APDs, modified from Webb et al. [28].

Here we discuss the p-on-n structures with a peak sensitivity in the 'blue' region. The n-on-p structure is basically a mirrored construction with highest sensitivity for red light.

The basic structure of these APDs is shown in the top row of figure 7, the electric field distributions as a function of depth for all three devices in the middle and the corresponding multiplication at the bottom. Electrons in both the beveled edge and the reach-through structure have high multiplication rates throughout almost the entire device structure while hole multiplication is kept to a minimum. In the reverse APD, by contrast, photoelectrons must be generated in front of the p-n junction buried at a depth of few micron to undergo multiplication. Full amplification can only be achieved when the diode is illuminated by blue light which has a very short absorption length of less than 1 μm.

The size of APDs is limited due to the production yield to achieve an extremely uniform field distribution over the sensitive area. The biggest area available commercially is 2.5 cm^2.

Advanced Photonix Inc. was the first to bring a large area APD on the market. The APDs have beveled edges to reduce the surface currents. It has a traditional p-n junction, in which the n-type resistivity is chosen so as to make the breakdown voltage very high ($\sim$2000 V). Due to a neutron transmutation process (the naturally occurring and uniform distributed ^{30}Si isotope is converted to P), the internal field and the gain are very uniform. Consequently, an excellent energy resolution of 4.3% FWHM for the 662 keV line from ^{137}Cs has been measured with this so-called Large Area Avalanche Photo Diode (LAAPD) from Advanced Photonix in combination with a YAP:Ce crystal [29] and 3.7% have been achieved in combination with a $LaCl_3$:Ce crystal [30]. The deep UV scintillation light of Argon (128 nm) has been detected with a LAAPD at a quantum efficiency greater than 40% [31].

A reach-through APD has a wide low-field drift region ($>$100 μm) at the front of the device and the multiplying region at the back. Almost the full thickness is active and also soft X-rays below 20 keV can be detected with good energy resolution [32]. Since most of the thermally generated dark current inside the thick p layer undergoes electron multiplication, large area devices tend to be noisy.

2009 JINST 4 P04004

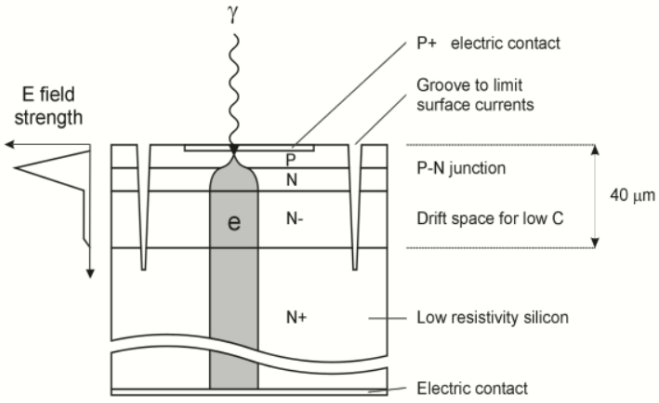

Figure 8. Structure of the Hamamatsu S8148 APD used by CMS.

Both APD types, the beveled edge and the reach-through, show a strong nuclear counter effect and can relatively easily be damaged by radiation.

The third type, the reverse APD has its p-n junction close to the front surface. An example is the APD developed for the CMS electromagnetic calorimeter [33].

The basic structure is low resistivity silicon with an epitaxial grown layer of low doped n-silicon on top. In this top layer with a thickness of 40 to 50 μm, the p-n junction is created by diffusion and ion implantation at a depth of ~ 5 μm. About 30 to 40 μm of the epitaxial grown layer of low doped n-silicon remains unaltered and acts only as a drift region but this reduces the capacitance and, consequently, the noise of the device. A groove close to the edge of the device prevents the flow of surface currents (figure 8).

The reverse APD has a number of advantages:

- small nuclear counter effect because of a very thin (typically < 5 μm) active layer before the multiplication zone
- good radiation hardness
- fast response
- small dark current
- reduced temperature dependence

4.2 Quantum efficiency

The QE of an APD is similar to the QE of a PIN photodiode (figure 5) but only photoelectrons created in front of the shallow p-n junction undergo full amplification while those produced close to the junction or behind see only part of the potential and thus the amplification is reduced. The holes contribute little because they have a much smaller ionization coefficient than electrons at the same field strength. Photons with long wavelengths often penetrate deeper into the silicon and the photoelectrons have, therefore, less chance to undergo full amplification, see figure 9 [34].

2009 JINST 4 P04004

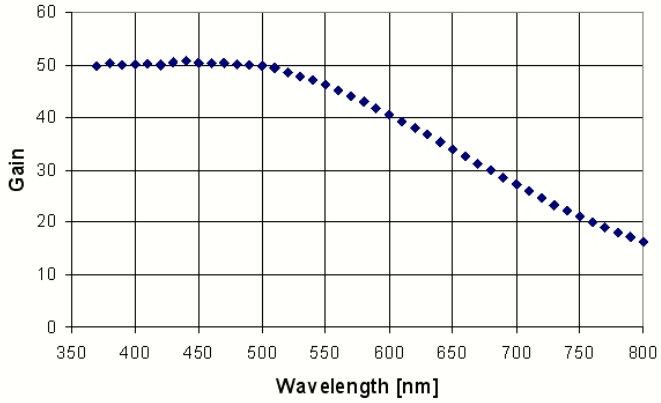

Figure 9. Gain of a reverse type APD (Hamamatsu S8148) as a function of the wavelength of the incident light. Measurement by Y. Musienko (INR (Moscow) and Northeastern Univ. (Boston)).

4.3 Nuclear counter effect

Electrons produced in the p-layer of 5 μm thickness (figure 8), either by photo-conversion or by ionizing particles traversing the APD, induce avalanche amplification at the p-n junction. Electrons created behind the junction by ionizing particles are collected but not amplified. The holes contribute little because of their much smaller ionization coefficient. The net effect for a traversing MIP can be expressed by an effective thickness, which is ~ 6 μm in the case of the APD S8148 developed by Hamamatsu Photonics for the CMS electromagnetic calorimeter [33]. The nuclear counter effect is about 50 times smaller than in a state of the art 300 μm thick PIN photodiode.

4.4 Excess noise factor

The avalanche multiplication in an APD is a stochastic process. The fluctuations are described by the excess noise factor F. In theory, it is for high gain (>10) mostly attributed to the contribution of the holes to the multiplication [35].

$$F = k_{eff} \cdot M + (2 - 1/M) \cdot (1 - k_{eff}) \tag{4.1}$$

$$\text{for } M > 10: \quad F = 2 + k_{eff} \cdot M \tag{4.2}$$

$$k_{eff} \approx k = \beta/\alpha \tag{4.3}$$

α and β are the ionization coefficients for electrons and holes, $\alpha \gg \beta$ in APDs biased below breakdown.

The theoretical lower limit of F at small gain is 2. It increases linearly with the gain and is $\sim$10 at a gain of 1000 (figure 10).

4.5 Stability

The gain of an APD exponentially depends on the bias voltage and, therefore, the relative change of the gain with voltage is a linear function of the gain. At a gain of 50, the relative change is $\sim$3.1% per volt and increases linearly to more than 30%/V at gain 1000. Similarly, the gain depends on temperature changes, which are caused by the energy loss in interactions of the electrons with

2009 JINST 4 P04004

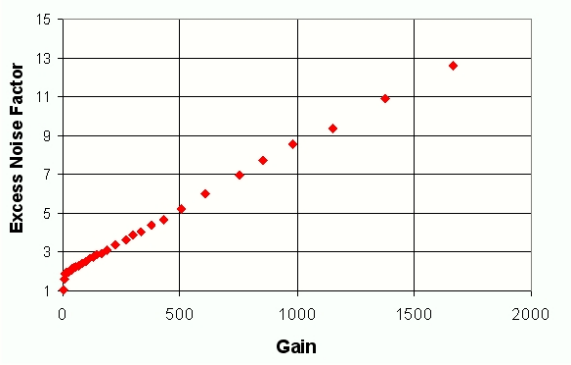

Figure 10. Excess noise factor for different gains (Hamamatsu APD, type S8148). Reprinted from [36].

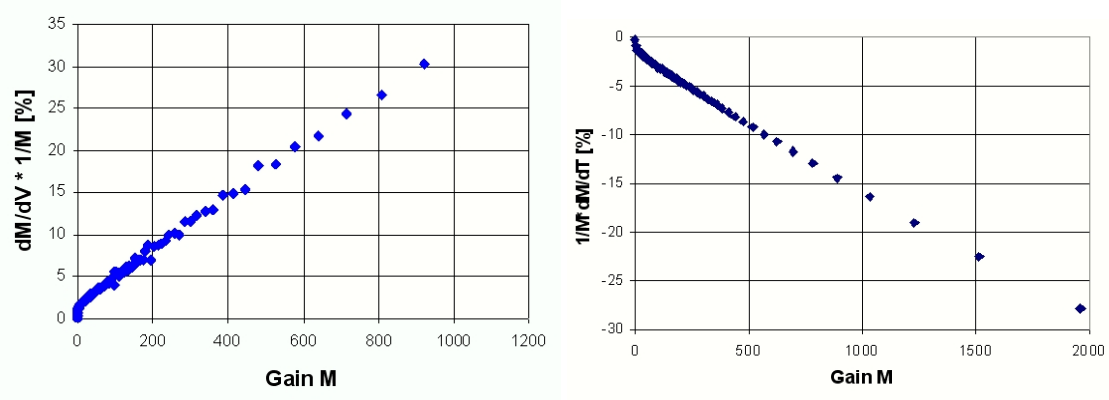

Figure 11. Relative change of the gain for variations of the bias voltage (left) and the temperature (right) plotted as function of the gain for the Hamamatsu S8148. Reprinted from [37].

phonons. The relative change is -2.4%/°C at gain 100 and -15%/°C at gain 1000 (fig 11, all values for the S8148 APD from Hamamatsu [37]). Because of the strong sensitivity to small changes in the bias voltage and temperature when operated close below the breakdown voltage, APDs have to be operated at moderate internal gain and need low noise preamplifiers.

4.6 Contribution of the APD parameters to the energy resolution

In a calorimeter with an APD as readout element, the APD contributes to all 3 conventionally used terms describing the energy resolution.

$$\frac{\sigma_E}{E} = \frac{a}{\sqrt{E}} \oplus b \oplus \frac{c}{E} \tag{4.4}$$

In detail, APDs contribute to the stochastic term a of the energy resolution of a crystal-APD system with their area (mismatch of the APD area and the crystal face), the quantum efficiency and the excess noise factor. The gain sensitivity to voltage and temperature variation increases the constant term b and the capacitance, serial resistance and dark current all add to the noise term c.

The dark current of state of the art APDs is very small and the excess noise factor is close to the theoretical limit as long as the gain is not too high. Therefore, the parallel noise can only be

2009 JINST 4 P04004

improved by a short shaping time, which anyhow is needed in high rate calorimeters with state of the art scintillating crystals. Unfortunately, the short shaping time increases the series noise, which becomes the dominant part. The APD should have the lowest possible capacitance to achieve the best possible energy resolution. To first order, the ENC is expressed by equation (4.5) (from [38]):

$$ENC^2 \approx 2q \cdot \left(\frac{I_{ds}}{M^2} + I_{db} \cdot F \right) \cdot \tau + 4kTR_s \cdot \frac{C^2}{M^2} \cdot \frac{1}{\tau} \tag{4.5}$$

τ is the shaping time, q the electron charge, I_{ds} the dark surface current, I_{db} the dark bulk current created before the p-n junction, M is the gain, F the excess noise factor, R_s the series resistance of the APD and the amplifier input, C the capacitance of the APD and the amplifier input, k the Boltzmann constant and T the absolute temperature.

4.7 Radiation hardness of reverse APDs

Most damage in reverse APDs, now commonly used in many HEP applications, is caused by non-ionizing energy loss, i.e. due to the creation of defects by the displacement of lattice atoms. Only a small amount of damage is caused by ionizing radiation and it mostly affects the surface, i.e. the interface of Si and SiO_2. The mean bulk current after irradiation with 2×10^{13} neutrons/cm^2 is $I_d \approx 280$ nA (Hamamatsu S8148, non-amplified value). This corresponds to 14 μA at gain 50 and amounts to a noise contribution of some 80 MeV being expected for the CMS calorimeter after 10 years of LHC operation with full luminosity [39].

Compared to PIN photodiodes the volume, which is relevant for the generation of the bulk current, is much smaller, i.e. it is only the area times the effective thickness. The value of the effective thickness is exactly the same as it was defined for the nuclear counter effect and is about 6 μm for the Hamamatsu APD S8148.

A damage parameter α has been measured with reverse APDs, which is slightly higher but consistent with the measurements for normal diodes [39]:

$$\alpha = (10 - 13) \cdot 10^{-17} \mathrm{A/cm} \tag{4.6}$$

In the case of a surface defect, for example caused by a dust particle during the production, the APD can be destroyed by ionizing radiation but not by neutrons which have little effect on the small volume of the surface structure. In order to ensure the reliability of the calorimeter of CMS, the APDs had been subject to a screening procedure, which included an irradiation with a dose of 5 kGy from a ^{60}Co source [40].

4.8 Arrays of APDs

Arrays are available from several manufacturers, mostly for applications in medical imaging (SPECT and PET). A monolithic array with 32 reverse APDs for example is produced by Hamamatsu Photonics [41], which was developed for a small animal PET scanner. The area of the individual APDs is 1.6×1.6 mm^2.

Radiation Monitoring Devices (RMD) produces arrays with up to 169 reach-through APDs of 1×1 mm^2 element size [42].

2009 JINST 4 P04004

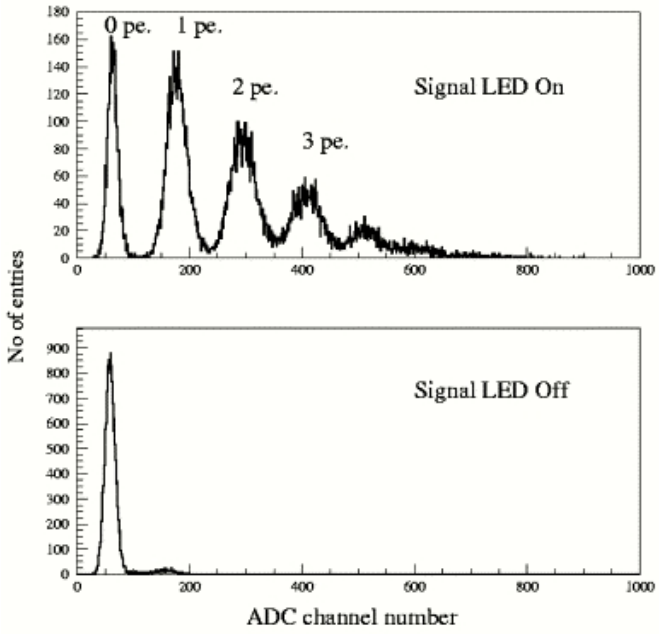

Figure 12. Typical pulse height distribution from a VLPC illuminated with weak signals from a LED (top) and response without illumination (bottom). Reprinted from [43].

5 The Visible Light Photon Counter (VLPC)

As a result of the efforts to develop semiconductor photosensors with single photon detection capabilities, a special variant of the APD, the so-called VLPC, has been developed. In the Rockwell International Science Center, Stapelbroek et al. developed the Solid State Photo Multiplier (SSPM) in 1987. This is an APD with very high donor concentration, which creates an impurity band 50 meV below the conducting band. Later, this device was modified to be less sensitive to infrared light and is now called the Visible Light Photon Counter (VLPC). The small band gap forces an operation at very low temperatures of a few degrees Kelvin.

VLPCs have, like Hybrid PMTs (HPD[1]) and G-APDs, an excellent sensitivity and resolution for single photons. They are fast and insensitive to magnetic fields but have to be operated at cryogenic temperatures. DØ is the only experiment that uses these devices in large quantity, in this case for the central fiber tracker, which consists of 80,000 fibers, partly 2.5 m and partly 1.7 m long [44]. The light produced by charged particles crossing a fiber is transported via $\sim$10 m long optical fibers to VLPCs housed in a cryostat, which regulates the operation temperature (6 to 8 degrees Kelvin). The pulse height distribution for weak light flashes with a mean number of photons of $\sim$1 is show in figure 12 [43].

[1] The HPD is a vacuum photomultiplier with a electron-bombarded diode as anode instead of the normal dynode system. The typical acceleration voltage applied to photo electrons is 8 to 12 kV, resulting in a multiplication gain of few thousand.

2009 JINST 4 P04004

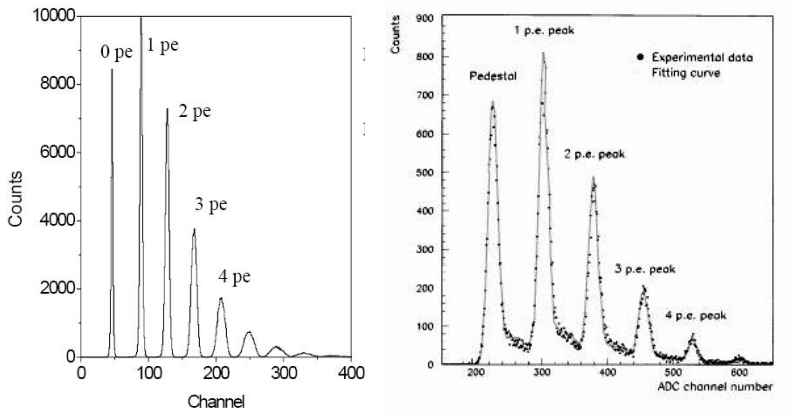

Figure 13. Pulse height spectrum of light pulses with very low intensity recorded with a G-APD (left) and a HPD. Reprinted from [45].

6 Geiger-mode Avalanche Photodiodes

At the beginning of this millennium the Geiger-mode avalanche photodiode (G-APD) has been further developed. This device can detect single photons just like a PMT with a very high gain first dynode and therefore some people call it a 'Silicon Photo Multiplier', (SiPM). The pulse height spectrum measured with a G-APD shows a resolution even better than what can be achieved with the best hybrid photomultiplier tubes (figure 13).

"Geiger-mode" describes the feature of these devices whereby a photo-generated carrier in the depletion region can trigger a diverging avalanche multiplication of carriers by impact ionization. Both positive and negative carriers (and also photons generated in the avalanche multiplication, see section 6.) are involved with a positive feedback effect, which, when the electric field is high enough, makes the carrier multiplication self-sustaining. In linear mode APDs, avalanches develop basically only in one direction (from the p- towards the n-material) and stop multiplying when the charge carriers reach the low field area of the n-zone. Very rarely are secondary avalanches started by holes or secondary photons in the p-layer. In G-APDs, the essential new process is the additional initiation of secondary avalanches, triggered by holes and secondary photons in the p-layer. A G-APD, therefore, does not turn off by itself and, as a consequence, the avalanche process must be quenched by the voltage drop across a high-ohmic serial resistor or by an active quenching circuit. Another important feature of G-APDs is that it is possible to bias small depleted volumes at the p-n junction well over the so-called breakdown voltage faster than on average a free electron is generated, which would lead to an avalanche breakdown, i.e. to keep small volumes for sufficient times in a supercritical state. It is obvious that large depleted volumes with a high electrical field could never be kept biased sufficiently long in time well over the breakdown voltage because sufficient free electrons would always be thermally generated. Initially, the idea to 'overbias' small, single volumes was tried in the 'Seventies of last century. It is obvious that semiconductors of low band-gap (except strongly cooled) or of high impurity will be completely unsuited for G-APDs because it is not possible to keep even very small depleted volumes free of charge carriers for suffi-

2009 JINST 4 P04004

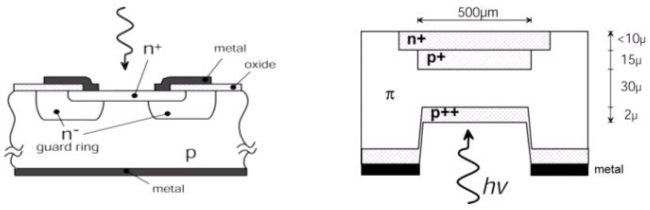

Figure 14. The first two silicon single photon detectors. The planar type from Haitz is shown on the left side and the reach-through type made by McIntyre on the right.

ciently long times. Also, it is obvious that materials with a high photon production (III-V materials for LED or laser diodes) are unsuited because, in the case of large secondary photon emission, secondary avalanches can be triggered in the entire ensemble of small cells by optical cross-talk

6.1 History

Pioneering work in the development of solid state single photon detectors, biased above the breakdown voltage, was carried out in the 'Sixties of the last century in the RCA company by R.J. McIntyre and co-workers [46] and by R.H. Haitz and his colleagues in the Shockley research laboratory [47]. Avalanche photodiodes operated in linear-(i.e. below breakdown bias) and in Geiger-mode (i.e. above the breakdown bias voltage) were, in the 'Sixties and early 'Seventies, a very active field of experimental and theoretical research. A model of the behavior was developed and verified with test structures (figure 14).

The performance of the first devices operated in Geiger-mode with a bias voltage several volts higher than the breakdown voltage was not very good but single photons were detected. The main problem was that only very small volumes of Si could be kept depleted for sufficient time above breakdown voltage to keep the diodes sensitive for photons. In most cases, the high internal bulk current in the depleted volume triggered an instant breakdown when the diode bias rose just above the breakdown voltage. Due to improved technologies it was possible to keep the depleted volume free of electrons for sufficiently long time biased well above breakdown. The development led to the so-called Single Photon Avalanche Diode (SPAD) and to the SLIK^{TM} structure produced by Perkin-Elmer [48]. The quenching of the breakdown was done passively by adding a high-ohmic series resistor similar to that used for Geiger counters in the early 'Twenties of the last century. The devices were therefore slow in recovering after a breakdown and in being charged up to the bias voltage, therefore the maximal count rate was smaller than 100 kHz. This is nowadays still the case for state of the art single cell devices. Only the development of active quenching circuits allows high count rates of more than 1 MHz and provides a short dead time [49].

A logical next step was to try to combine many small cells operated in the Geiger mode on a single wafer and either to use an external quenching element or to integrate it directly onto the wafer either near or directly onto the individual cells.

Radiation Monitor Devices Inc. (RMD) developed an array of APDs with single photon detection capability for DIRC applications (Detection of Internally Reflected Cherenkov light). It consists of 6×14 individual APDs with a size of 150×150 μm^2. It is operated in Geiger-mode and has an active quenching circuit for each APD [50].

2009 JINST 4 P04004

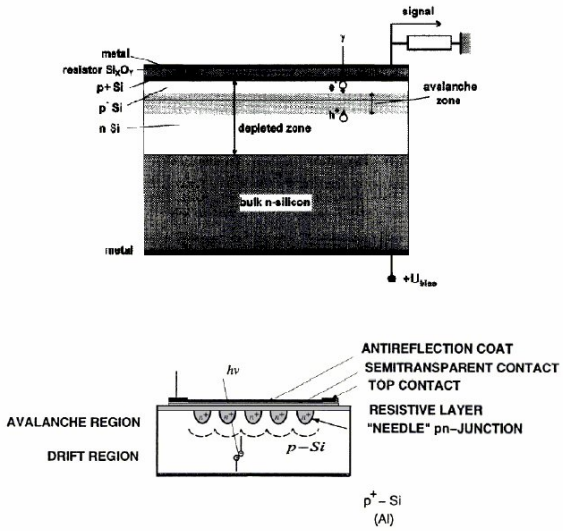

Figure 15. Examples of MRS APD structures. The picture on top is reprinted from [51] and the picture at the bottom is reprinted from [52].

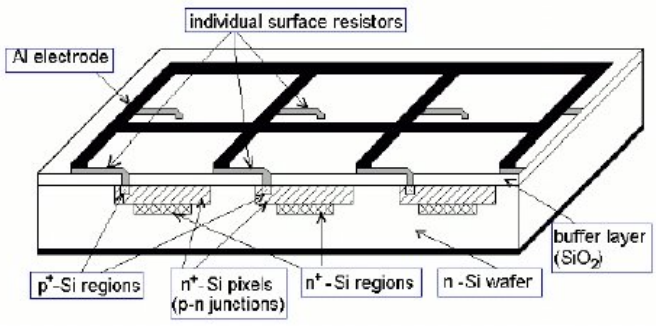

Figure 16. Basic structure of a Geiger-mode avalanche photodiode. Sketch by Z. Sadygov (JINR Dubna).

Around 1990, the MRS (Metal-Resistor-Semiconductor) APDs were invented in Russia. A very thin metal layer (Ti,$\sim$ 0.01 μm) and a layer of SiC or Si_XO_Y with a resistivity of 30 to 80 MΩcm limits the Geiger breakdown by a local reduction of the electric field. The technology is difficult because all parameters need to be controlled very precisely. Two examples [51, 52] out of a large number of different designs are shown in figure 15.

The next step was logical: subdivide the MRS structure into many cells and connect them all in parallel via an individual limiting resistor (figure 16). The Geiger-mode avalanche photodiode (G-APD) was born. Key personalities in this development were V. Golovin [53] and Z. Sadygov [54]. The G-APD is produced by a standard MOS (Metal-Oxide-Silicon) process and promises eventually to be relatively simple and therefore cheap.

Quite different configurations and structures are possible and new developments are ongoing with high intensity. Nowadays, quite a few first generation commercial devices are available; nevertheless, the required level of maturity of PIN photodiodes has still not been reached. Many devices produced commercially are constructed like the example shown on top of figure 17. The

2009 JINST 4 P04004

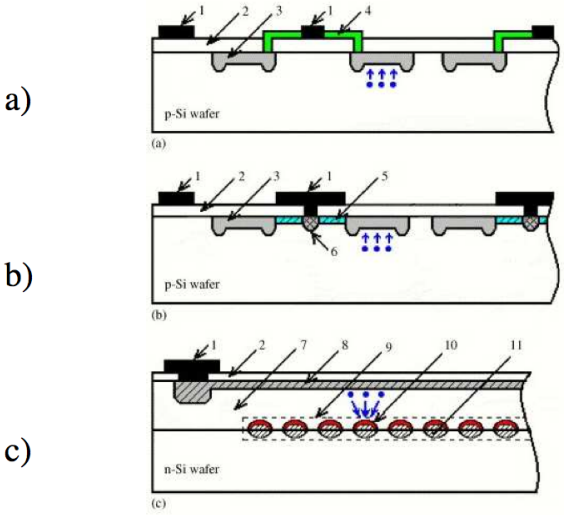

Figure 17. Schematic views of the so-called Multi-pixel Avalanche PhotoDiode (MAPD): (a) the MAPD with individual surface resistors; (b) a special version dubbed AMPD with surface transfer of charge carriers; (c) the MAPD with individual micro-wells. 1—common metal electrode, 2—buffer layer of silicon oxide, 3—p–n junctions/micro-pixels, 4—individual surface resistors, 5—individual surface channels for the transfer of charge carriers, 6—drain region/contact, 7—epitaxial silicon layer of p-type conductivity, 8—a high-doped silicon layer of p-type conductivity, 9—a region with micro-wells, 10—local avalanche regions, 11—individual micro-wells. Reprinted from [55].

other 2 versions (middle (b) and bottom (c) of figure 17) are only produced by Z. Sadygov, Dubna and Zecotek. Version (c) of figure 17 in particular allows a very high cell density. Devices with up to 40,000 cells/mm^2 are nowadays available.

6.2 Properties of G-APDs

6.2.1 High gain

G-APDs produce a standard signal when any of the cells goes to breakdown. The amplitude A_i is proportional to the capacitance of the cell divided by the electron charge times the overvoltage.

$$A_i \sim C/q(V - V_b) \tag{6.1}$$

V is the operating bias voltage and V_b is the breakdown voltage.

When many cells are fired at the same time, the output is the sum of the standard pulses

$$A = \sum A_i \tag{6.2}$$

The gain is typically in the range of 10^5 to 10^7 but there also exist designs with only a gain of 10^4 (see later discussion) Single photons produce a signal of several millivolts on a 50 Ohm load (figure 18). No (or at most a simple) amplifier is needed for many applications for single photon detection. Particularly low-level light detection with PIN photodiodes or linear mode APDs requires high quality shielding to prevent pickup. Because of the extremely small extension of the cell size and the high gain, G-APDs have practically no pickup noise and often need no shielding

2009 JINST 4 P04004

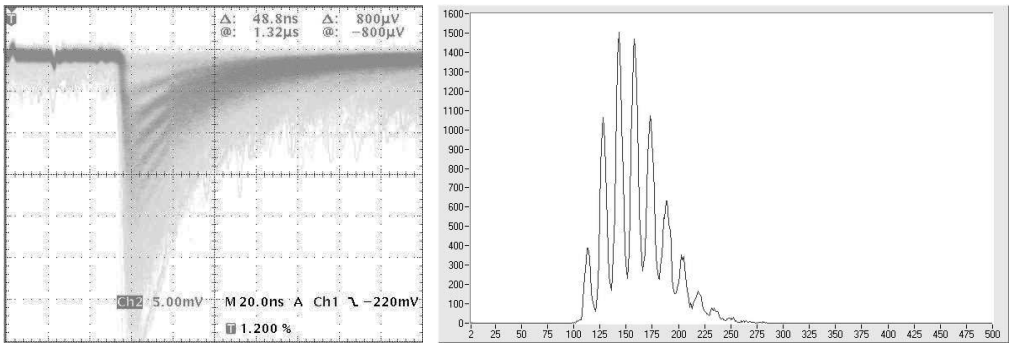

Figure 18. Left: Oscilloscope picture of the signal from a G-APD (Hamamatsu 1-53-1A-1) recorded without an amplifier. Right: The corresponding pulse height spectrum. Vertical and horizontal scale in arbitrary units.

at all (see later example of a combined PET NMR detector in medical applications, see section 6). Contributions from the Nuclear Counter effect are absolutely negligible — even a heavily ionizing particle passing a cell produces a signal, which is not bigger than that of a photon or a noise count. Since there are no avalanche fluctuations as in normal APDs, the excess noise factor is very small and it could eventually be negligible if other contributions from optical crosstalk can be suppressed. Groom's theorem [56] is not valid. This theorem states that the resolution of an assembly of a scintillator and a semiconductor photo detector is independent of the area of the photon detector because, in first order, the photon statistic improves linearly with the photo detector area while equally the noise increases linearly with the detector capacitance, which is again proportional to the area.

The output signal is proportional to the number of fired cells as long as the number of photons in a pulse (N_{photon}) times the photo detection efficiency (PDE) is significant smaller than the number of cells N_{total} (figure 19). Equation (6.3) is not exact but describes the data very well.

$$A \approx N_{\text{firedcells}} = N_{\text{total}} \cdot \left(1 - e^{-\frac{N_{\text{photon}} \cdot \text{PDE}}{N_{\text{total}}}}\right) \tag{6.3}$$

Two or more photons, which convert within the same time in one cell produce exactly the standardized signal of 1 single photon. When the number of impinging photons times the PDE exceeds 50% of the available cells, the deviation from linearity is more than 20%.

An important issue in G-APDs for the detection of photons is the strong dependence of the PDE as a function of the overvoltage. To highlight the problem one could compare the PDE with that of PMTs. The gain of a PMT can be varied over a wide range by increasing or decreasing the applied high voltage. The PDE, which in the case of a PMT is the QE times the probability that the primary photo-electrons reach the first dynode and are successfully amplified, is only weakly dependent on voltage changes. (In most demanding conditions in order to decouple the PDE completely from the gain adjustments a fixed voltage is used between the cathode and the first dynode while one only varies the voltage across the later dynodes). In contrast, the gain of G-APDs strongly influences the PDE due to two main processes, a) the voltage-dependent probability to trigger the initial avalanche and b) the gain-dependent increase in optical crosstalk, which fakes larger signals and eventually will limit the operation of the G-APD at very high gains. The

2009 JINST 4 P04004

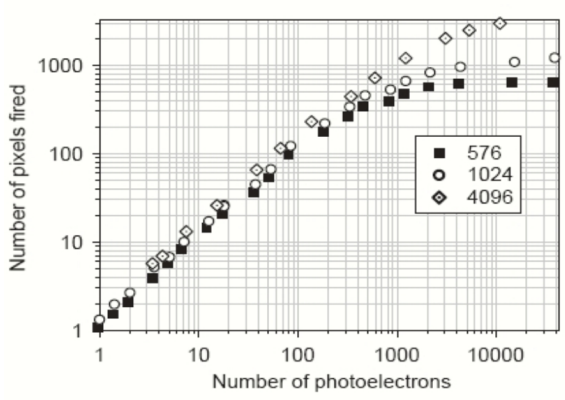

Figure 19. Nonlinear response to a 40 ps laser light signal for G-APDs with different number of cells. Reprinted from [57].

gain of G-APDs is, on one hand, more or less fixed for a given structure, mainly by the area and by this the capacitance of the individual cells and, on the other hand, set by the overvoltage V_{OV} (V_{OV} = V_{bias} − $V_{breakdown}$ = V — V_b). Any change of the bias voltage will change the gain and, at the same time, will therefore have a serious influence on the PDE (see section 6.2.4 for a detailed discussion). Often, the limitations by optical crosstalk and variations in gain will limit the achievable PDE well below the QE. Ignoring this correlation and the subsequent reduction in PDE can lead to misunderstandings of the performance of G-APDs.

6.2.2 Sensitivity of the gain to the bias voltage stability

The G-APD signal stability depends mainly on a) the stability of the applied bias and b) on temperature changes (see next section). To describe the dependence of the G-APD response on the bias voltage one can introduce a voltage dependent coefficient k_V(V) as follows:

$$k_V(V) = \frac{1}{A} \cdot \frac{dA}{dV} \cdot 100\% \tag{6.4}$$

Examples of the voltage dependence are shown in figure 20. The amplitude A of the signals of 2 G-APDs from Hamamatsu and Photonique/CPTA have been measured and the coefficients derived (figure 20) [58]

For precision measurements, the voltage has to be regulated at the diode and not before the bias resistor to avoid gain drops due to large temporary light signals, resulting in current changes in the resistor and, in turn, a voltage drop.

6.2.3 Temperature dependence of the gain

The breakdown voltage of a silicon diode depends strongly on the temperature because of the interactions of the carriers with phonons. Almost all parameters of a G-APD are a function of the overvoltage V-V_b. Here we discuss the influence of temperature changes on the gain. Similar to the coefficient k_V(V), which describes the dependence on the bias voltage we define:

$$k_T(V) = \frac{1}{A} \cdot \frac{dA}{dT} \cdot 100\% \tag{6.5}$$

2009 JINST 4 P04004

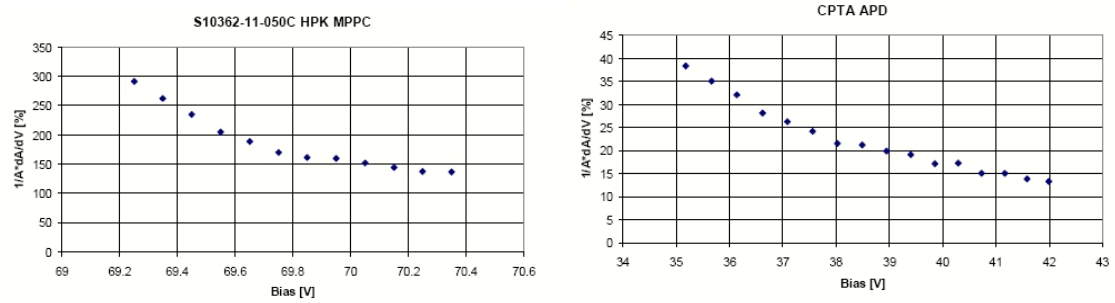

Figure 20. Voltage coefficients $k_V(V)$ of a G-APD from Hamamatsu (left) and from Photonique/CPTA (right) depending on the bias voltage at T=22 °C. Reprinted from [58].

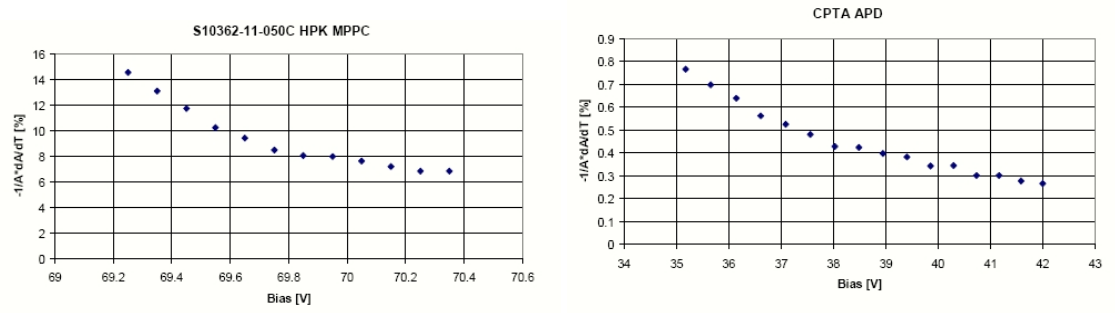

Figure 21. Temperature coefficients of a G-APD from Hamamatsu (left) and from Photonique/CPTA (right) as function of the bias voltage. Reprinted from [58].

Again the amplitudes A of the signals of 2 G-APDs from Hamamatsu and Photonique/CPTA have been measured at different temperatures and the coefficients derived (figure 21) [58]

For a stable operation, the temperature needs to be controlled with a precision of a fraction of a degree. Alternatively, the applied bias voltage has to be corrected to compensate for the shift of the breakdown voltage caused by temperature changes.

For the device from Hamamatsu, the bias voltage needs to be increased by ∼50 mV when the temperature rises by 1 °C if the device is operated with at least a $V_{OV} > 1$ Volt while for the Photonique/CPTA device the compensation is ∼20 mV/°C for $V_{OV} > 1$ Volt.

6.2.4 Photon Detection Efficiency (PDE)

The PDE is the product of a) the quantum efficiency (QE) of the active area, b) the geometric fill factor ε (ε = ratio of sensitive to total area) and c) the probability that an incoming photon triggers a breakdown (P_{trigger}). A small correction that the hit cell is still recovering from a previous breakdown (from noise or a previous light signal) is neglected in current discussions[2]

$$\text{PDE} = \text{QE} \cdot \varepsilon \cdot \text{P}_{\text{trigger}} \tag{6.6}$$

The geometric factor ε needs to be optimized depending on the application. Since some space is needed between the cells for separation and the individual resistors, the best filling can be

[2] We assume also that the lifetime of the free carriers in the depletion layer is much longer than the time needed for the acceleration.

2009 JINST 4 P04004

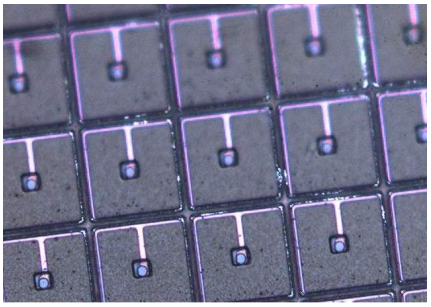

Figure 22. Magnified photo of a G-APD produced by Photonique/CPTA.

achieved with a small number of big cells. For example, for cameras of air Cherenkov telescopes for ground based γ-ray astronomy or a ring image Cherenkov counter (RICH) in HEP applications, the highest possible PDE is wanted. Since in this case the number of photons is small, big cells are suitable and a geometric fill factor of 70% or more is possible. Nevertheless, too large a cell size has generally the disadvantage of a low dynamic range and larger dead-time due to the accumulation of 'dead' cells caused by the more frequent noise triggers in the larger depleted volume. The increase in volume of the cells is eventually limited by the thermally generated electron-hole pairs because the generation rate is proportional to the depleted volume. Therefore, in combination with the recovery time of the cells, given by the capacitance and the value of the individual quenching resistor, the thermal generation sets an upper limit to the volume of the cells.

An example of the need for a large number of cells is PET. One of the preferred materials for PET nowadays, Lutetium Oxyorthosilicate (LSO) crystals, produce many photons ($\approx$ 15000 per a 511 keV X-ray) and up to a few 1000's can be collected at the end face of the crystals. In order to avoid a saturation effect, the number of cells needs to be big for the given viewing area and, in turn, the cells must be small. The currently achieved geometric fill factor ε in suitable models is in the range of 40 to 60%. An example is shown in figure 22.

The triggering probability depends on the position where the primary electron-hole pair is generated. Compared to holes electrons have a better chance in silicon to trigger a breakdown. Therefore, a conversion of the photon in the p-layer has the highest probability to trigger a breakdown. This has been calculated by W.G. Oldham et al. [59]. They define an avalanche region with width W and the position x, which runs from 0 to W starting at the n-edge (figure 23).

Oldham and co-workers verified their calculations by illuminating a diode with short (390 nm) and long (1050 nm) wavelengths and achieved good agreement.

The triggering probability can be calculated following [60]

$$\frac{dP_n}{dx} = (1-P_n)\cdot\alpha_n\cdot(P_n+P_p-P_nP_p) \tag{6.7}$$

$$\frac{dP_p}{dx} = -(1-P_p)\cdot\alpha_p\cdot(P_n+P_p-P_nP_p) \tag{6.8}$$

$P_n(x)$ is the probability that an electron starting from the position x inside the depletion volume with the width W triggers a breakdown and $P_p(x)$ is the same probability for holes. α_n and α_p are the ionization coefficients for electrons and holes. The total triggering probability P_t can be calculated by integrating the equations with the boundary conditions that $P_n(0)=0$ and $P_p(W)=0$

2009 JINST 4 P04004

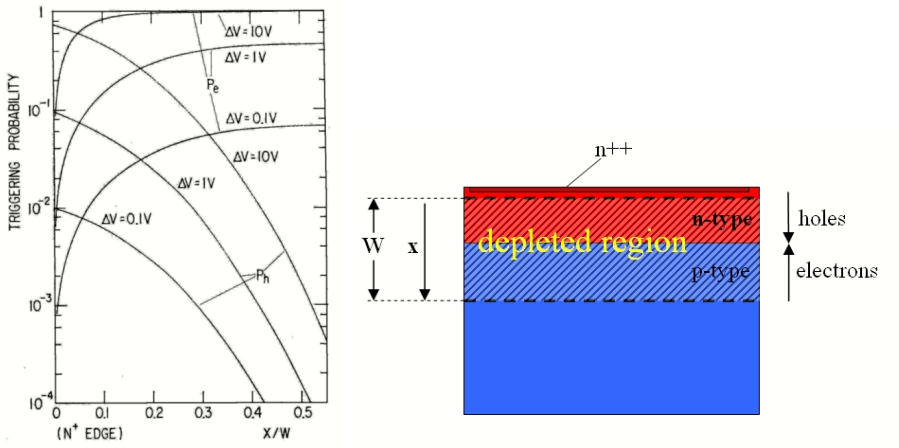

Figure 23. Triggering probability for different positions of carrier generation (left, see text, modified [59]) and sketch of the structure for an explanation of the parameters W and x (right).

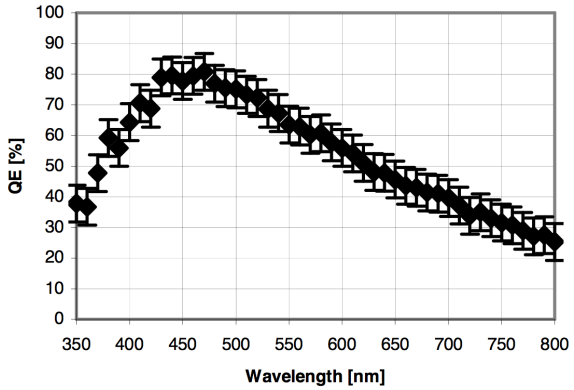

Figure 24. Quantum efficiency of the active area as function of the wavelength for Hamamatsu 0-50-2 with 400 cells/mm^2. The error bars denote the systematic measuring error.[3]

(the probability to trigger a breakdown is zero for carriers exiting the high field region). P_t depends on the shape of the electric field and hence on the doping profiles. It always increases with the applied excess bias voltage (V-V_b).

The QE of the active area can reach 80 to 90% depending on the wavelength. It peaks in a relatively narrow range of wavelengths compared to the QE distribution of a PIN diode (figure 24) because the sensitive layer of silicon is very thin. In the case shown in figure 24, the G-APD structure is p-silicon on an n-substrate. The p-layer is 0.5 μm thick on a 4 μm epitaxial n-layer.

G-APDS with an n-on-p structure operated just above the breakdown voltage V_b are inefficient for short wave length photons because these photons must penetrate into the p layer to generate electrons that initiate avalanches when moving towards the n-layer. When raising the voltage well above V_b then holes, generated by short wavelength photons in the n-layer, will be able to initiate

[3]The unpublished measurements shown in this figure and in figure 26 have been done by Y. Musienko (INR (Moscow) and Northeastern University (Boston)) and some in the following figures without a reference (figures 28, 30, 33 and 42) by D. Renker.

2009 JINST 4 P04004

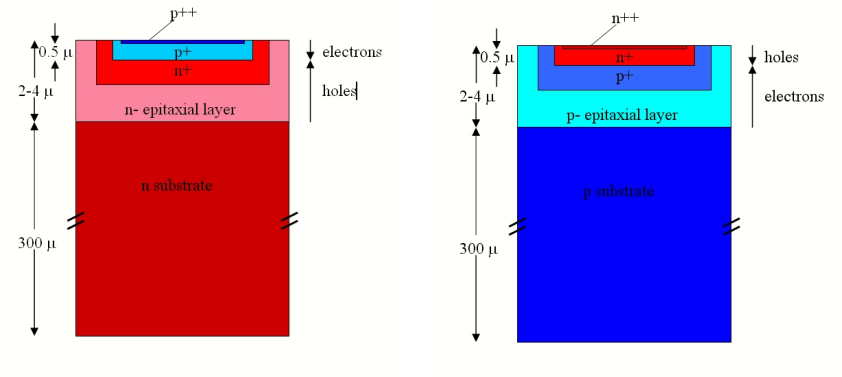

Figure 25. Simplified schematic view of one cell of a G-APD. Not shown are the passivation layers, the quenching resistors and the Al connection lines. Left is the so-called p-on-n structure (predominantly blue-sensitive) and right the n-on-p (predominantly red-sensitive) structure.

a measurable signal. According to figure 23, a much higher overvoltage is required to obtain a reasonable blue-sensitivity of n-on-p structures compared to that required in the case of a p-on-n structure [59].

G-APDs are produced in the following way: At first, a thin epitaxial layer (2 to 4 μm) is grown on a wafer (typically 300 μm thick) of low resistivity, which is needed for the handling but has no other function. The first step towards a p-n junction is the diffusion of dopants with high concentration into the epitaxial layer. So far all layers - the wafer (substrate), the epitaxial layer and the heavily doped volume created by diffusion - are of the same type of silicon, n-type or alternatively p-type. The junction is then formed some 0.5 μm below the surface by a shallow diffusion (or ion implantation) with the opposite dopant. In a final step, an extremely thin but heavily doped layer is created on the surface, which distributes the potential uniformly over the whole area of the diode. Further production details like provisions to suppress the surface currents, the passivation of the surface with SiO_2, the creation of polysilicon quenching resistors and the aluminization are omitted here. The final structure is schematically shown in figure 25.

The so-called p-on-n structure (left pane in figure 25) will be preferentially sensitive to blue light, which is absorbed in the first fraction of a μm (see figure 2 for the absorption length of light in silicon) An electron-hole pair is created but only the electron will drift to the high field of the p-n junction and trigger a breakdown with high probability. Photons with longer wavelengths, in contrast, will mostly be absorbed in the n-layers behind the p-n junction and holes will drift towards the junction. They have a smaller triggering probability and consequently their PDE will be reduced (figure 26).

The situation is opposite for the n-on-p structure (right pane in figure 25). Photons with short wavelengths have a reduced PDE and the peak PDE is shifted to longer wavelengths up to ~550 to 600 nm (figure 27).

The PDE depends on the overvoltage (figure 28). Operation at high gain (high bias voltage) is favored but, in most cases, a compromise needs to be found because at high gain the dark currents and the dark count rate become very high and the optical crosstalk increases.

A semiconductor material other than silicon, in which the carriers have a higher mobility and

2009 JINST 4 P04004

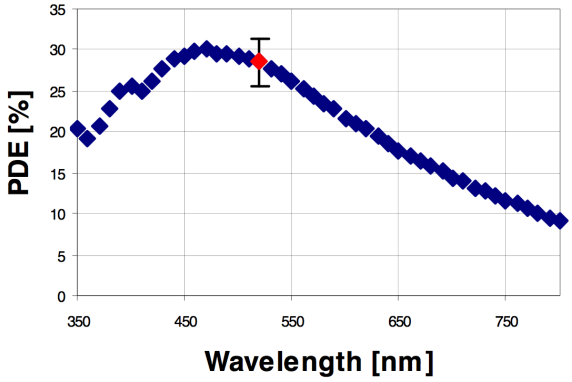

Figure 26. PDE of a so-called p-on-n G-APD produced by Hamamatsu (PSI-33-050C) operated 1 V over the breakdown voltage. The red data point with error bars indicates the size of the systematic error.

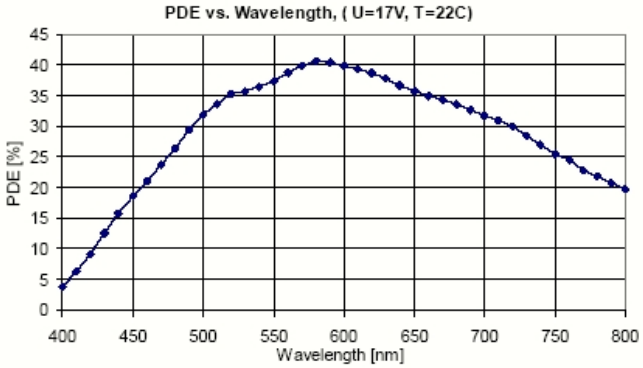

Figure 27. PDE of an n-on-p G-APD produced by Photonique/CPTA (SSPM_0710G9MM) operated some 4 V over the breakdown voltage [61].

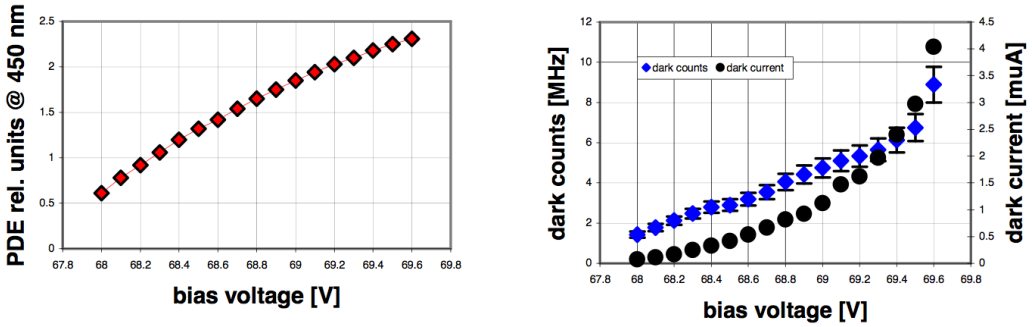

Figure 28. PDE of Hamamatsu MPPC-33-050C as function of the applied bias voltage in relative units (left pane) and the dark currents and dark counts measured at 25°C in the same voltage range (right pane).

higher ionization coefficient, like GaAs, could have a very high trigger probability but, on the other hand, a much higher optical crosstalk due to a high production of photons in the avalanche process (GaAs is a direct bandgap material)

2009 JINST 4 P04004

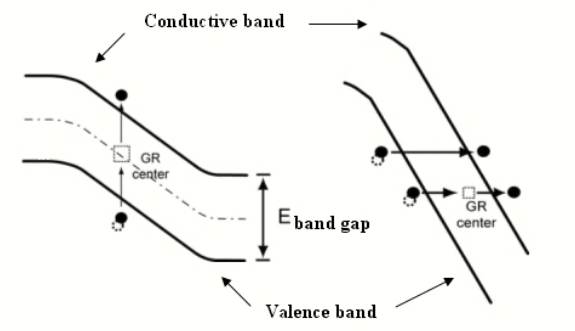

Figure 29. Thermally (left) and field-assisted generation (right) of free carriers, which can trigger a breakdown.

6.2.5 Dark counts

A breakdown can be triggered by an incoming photon or by any generation of free carriers in the depleted layer of a few micron thickness (figure 29). The latter produces dark counts with a rate of 100 kHz to several MHz per mm^2 at 25°C and with a threshold at half of the one photon amplitude. Two main processes are responsible for dark counts, thermally generated e-h pairs and so-called field-assisted generation of free electrons.

Thermally generated free carriers can be reduced by cooling. There is a factor 2 reduction of the thermally generated dark counts every 8°C drop in temperature.

Field-assisted generation without the help of a phonon (trap-assisted tunneling [62, 63]) has, compared to the thermal generation, a relatively small effect. It can only be reduced by operating the G-APDs at a smaller electric field, thereby lowering the gain and reducing the PDE.

The dark counts can be influenced by the G-APD production process aiming to minimize the number of generation-recombination centers (GR center), the impurities and crystal defects, which give rise to the Shockley-Read-Hall process.

Dark count events can have amplitudes twice or even several times higher than the amplitude of a single cell breakdown. The responsible effect, the optical crosstalk, will be discussed in the next section.

The count rate falls dramatically when increasing the threshold of the readout electronics. Each increase of the threshold by the equivalent of the 1 photo-electron amplitude reduces the noise count rate by almost one order of magnitude (figure 30). When the threshold is set to a value higher than the 4-photoelectron amplitude, the dark count rate is below 1 kHz.

In first order, the thermal generation of carriers is proportional to the depleted volume, which, for every cell, is the area times the thickness of all the layers on top of the low-ohmic substrate. In the p-type layers, the electrons and, in the n-type layers, the holes drift towards the high field region of the junction. The electrons will trigger a breakdown with higher probability than the holes. In standard p-on-n type G-APDs, the thickness of the p-layer is normally much thinner than in the n-on-p G-APD (see figure 25). Consequently, the lowest rate of dark counts can be expected for the p-on-n type G-APD (left pane of figure 25).

2009 JINST 4 P04004

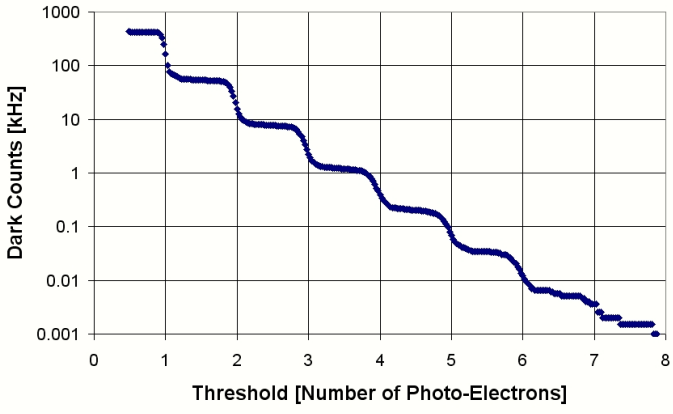

Figure 30. Dark count rate for different values of the discriminator threshold. The G-APD used in this measurement is the S10362-11-050C from Hamamatsu operated at a gain of $7.5 \cdot 10^5$.

6.2.6 Optical crosstalk

In an avalanche breakdown, there are on average 3 photons emitted per 10^5 carriers with photon energy higher than 1.14 eV, the band gap of silicon [64]. When these photons travel to a neighboring cell they can trigger a breakdown there (figure 31), like any external photon. This effect is called optical crosstalk. Particularly critical are photons in the spectral range of some 850 to 1100 nm [65] because higher energy photons are practically all absorbed within the same cell and infrared photons with wavelengths longer than 1100 nm travel over long distances without being absorbed.

Several models were suggested in the past for explaining the light emission, for example, bremsstrahlung and a multimechanism scenario, including indirect and direct interband and intraband transitions (see for details [64, 66–70]).

The optical crosstalk acts like shower fluctuations in an APD. It is a stochastic process and introduces an excess noise factor F as in a normal APD or in a PMT. Neglecting saturation effects and contributions from afterpulses and dark counts in the wide gate needed for the measurement of light from a scintillating crystal F can be approximated:

$$F \approx 1 + p_{ct} \tag{6.9}$$

The probability p_{ct} is defined by the rate of dark count events with crosstalk (threshold 1.5 fired cells) divided by the total dark count rate (threshold 0.5 fired cells).

With a dedicated design, which has an additional junction and with grooves between the cells, which act as an optical isolation, the optical crosstalk can be reduced (figure 32) [72–74]. Operation at relatively low gain is advantageous to reduce optical crosstalk, albeit with the disadvantage of reducing the PDE significantly. A quite convenient alternative method to suppress optical crosstalk is to insert narrow grooves between cells and fill them with an optical absorber. The disadvantage is the need for space reducing the active area, i.e. reducing the filling factor ε and, in turn, the PDE.

A concern in compact scintillator-G-APD arrangements is that photons generated in a breakdown of a G-APD penetrate into a crystal that is coupled to the G-APD, are then reflected at the end of the crystal and come back to the G-APD where some additional cells might be triggered.

2009 JINST 4 P04004

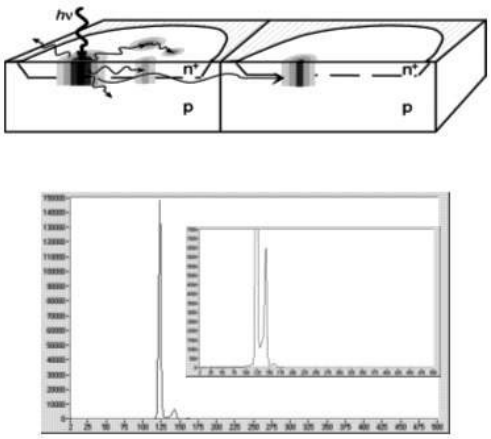

Figure 31. Optical crosstalk in a G-APD (top, sketch from [71]) and a pulse height spectrum of events triggered by one single carrier (bottom). Events where a second and even a third cell were fired are visible as satellite peaks. The insert is the same histogram but with the vertical scale expanded by a factor of 20 (S10362-11-050C from Hamamatsu).

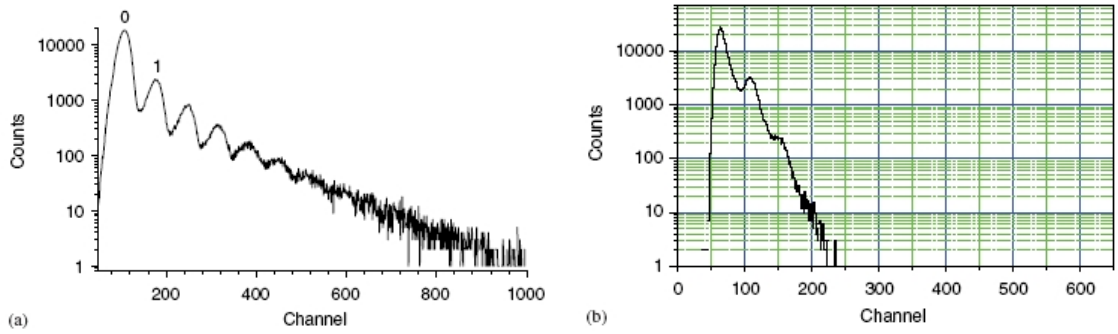

Figure 32. Optical crosstalk for 1×1 mm^2 G-APD produced by MEPHI/Pulsar, measured as the pulse height distribution: no suppression (a); with suppression of the optical crosstalk (b) by grooves. Reprinted from [73].

This effect was simulated by a reflector made of aluminized Mylar, which was mounted in front of a G-APD from Hamamatsu (type PSI-11-100C operated at a gain of $2.4{\cdot}10^6$) in order to simulate the emission into a crystal and reflection of the light at the other end of the crystal.

The peaks from dark counts with internal cross talk (2 or more cells fired) were enhanced by $\sim$18% (from 15.7% crosstalk probability to 18.6%) by reflected photons (figure 33). With a diffuse reflector (8 layers of Teflon foil) the enhancement was $\sim$12%.

The effect was also measured with 2 G-APDs (Hamamatsu MPPC HC050) mounted face to face (figure 34). The coincidence rate was determined as a function of the relative position of the 2 G-APDs. It amounts to some 1 kHz. The single G-APD dark count rate was 200 kHz [75].

The optical crosstalk depends strongly on the over-voltage and, consequently, on the gain, shown in figure 35 for the G-APD Hamamatsu S10362-33-050C. The gain at an overvoltage of 1.1 V is $6{\cdot}10^5$. A reduction of the optical crosstalk for the same cell area and fill factor can only be

2009 JINST 4 P04004

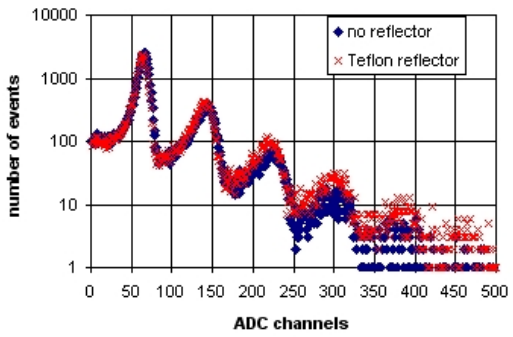

Figure 33. Spectrum of dark count events with and without a reflector made of aluminized Mylar in front of a G-APD (Hamamatsu PSI-11-100C) operated at a gain of $2.4 \cdot 10^6$.

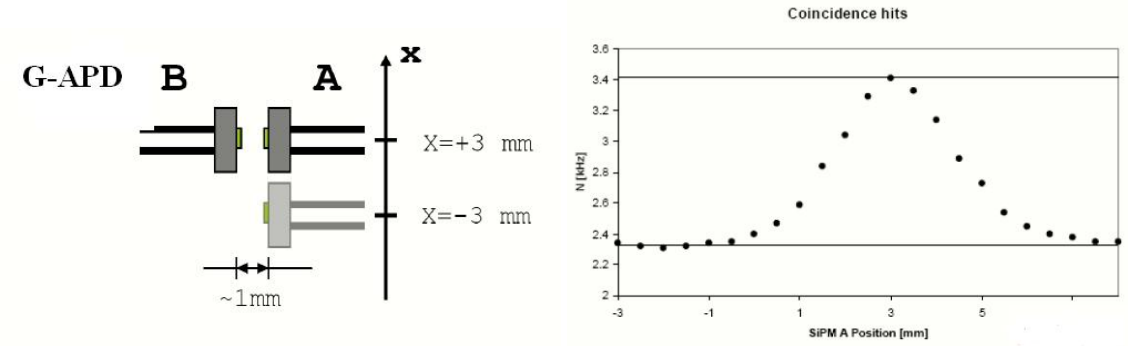

Figure 34. Coincidence events caused by the emission of light. Left, setup and right, the measured coincidence rate as function of the relative position. The lower line indicates the accidental coincidences. Reprinted from [75].

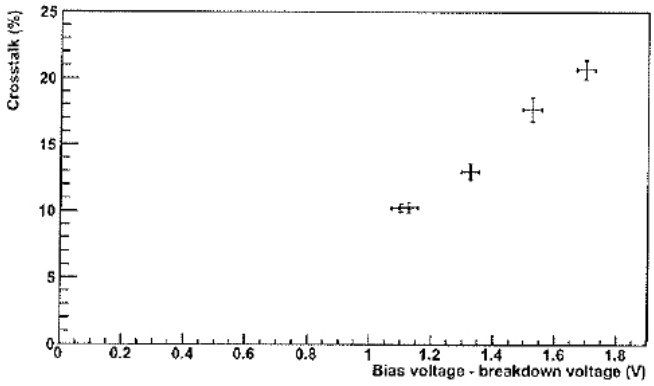

Figure 35. Measurement of the rate of dark count events with crosstalk (threshold 1.5 fired cells) in percent of the total rate (threshold 0.5 fired cells) at different bias voltages for Hamamatsu S10362-33-050C. Taken from [76].

achieved by reducing the cell capacitance, i.e. by an increase of the depleted volume, albeit with an increase in dark counts.

2009 JINST 4 P04004

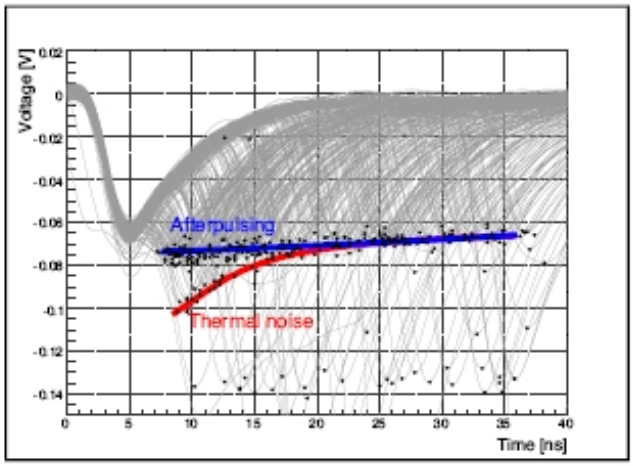

Figure 36. Superposition of events with the incidental pulses of an MPPC-11-050 from Hamamatsu (arranging the time origin to the peak of the original pulses). Also visible are the events with crosstalk at ∼-0.13 mV. Taken from [77]. Note: direct crosstalk events are suppressed by a special trigger.

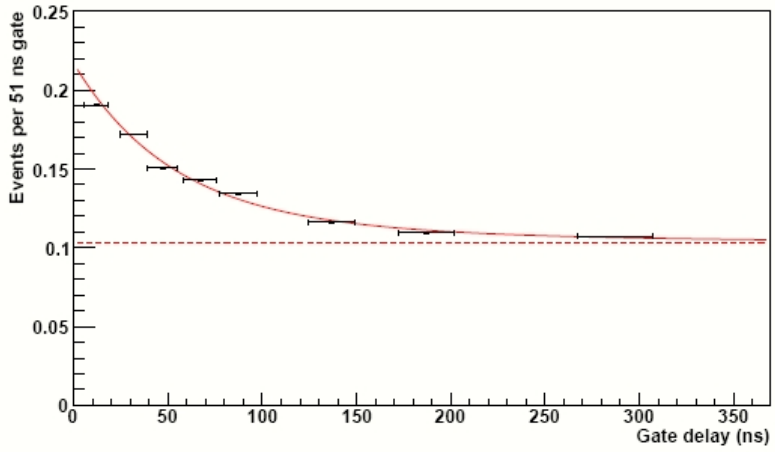

Figure 37. The probability for a delayed release of carriers as function of time after a breakdown event. The level of dark counts is indicated by the dashed line. Taken from [76].

6.2.7 Afterpulsing

In the silicon volume where a breakdown happened a plasma with high temperatures (a few 1000°C) is formed and deep-lying traps in the silicon are filled. Carrier trapping and delayed release causes afterpulses during a period of several 100 nanoseconds after a breakdown. Figure 36 shows an oscilloscope screen shot with dark counts and their crosstalk and afterpulse events.

The afterpulse probability of the device Hamamatsu S10362-33-050C has been measured by counting dark counts in a gate with fixed width but variable delay (figure 37). Two components have been found with a 50 ns and 140 ns time constant, respectively [76].

Afterpulses with short delay contribute little because the cells are not fully recharged but have an effect on the recovery time. Operations at low temperatures elongate the delayed release because

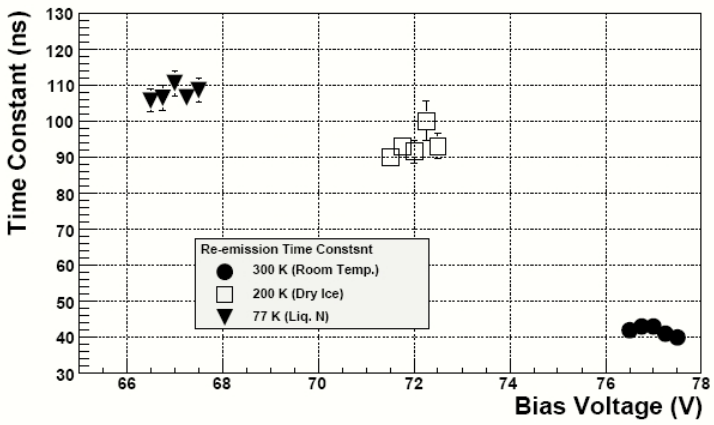

Figure 38. Time constant of afterpulses as a function of bias voltage at 3 different temperatures. Reprinted from [78].

Table 1. Recovery time and pulse decay time (1-1/e) for three different types of G-APDs from Hamamatsu. From [77].

Type Hamamatsu	**1600 cells/mm^2**	**400 cells/mm^2**	**100 cells/mm^2**
Bias voltage	V_b + 3.3 V	V_b + 2.7 V	V_b + .87 V
Recovery time	$\sim$ 4 ns	$\sim$ 9 ns	$\sim$ 33 ns
Pulse decay time	$\sim$ 5 ns	$\sim$ 11 ns	$\sim$ 35 ns

of the increase of the trapping center de-excitation time. Figure 38 shows the time average constant as a function of the bias voltage. At low temperatures, it is found to be longer than that at room temperature. The measurements show that the time constant is basically independent of the bias voltage at each temperature (figure 38) [78].

6.2.8 Recovery time

The time needed to recharge a cell after a breakdown has been quenched depends mostly on the cell capacitance and the individual quenching resistor ($\tau \sim$ RC). Afterpulses can prolong the recovery time because the recharging starts anew. This can be reduced only by operation at low gain. Some G-APDs need hundreds of microseconds after a breakdown until the amplitude of a second signal reaches 95% of the first signal. The shortest recovery times have G-APDs with small cells and small resistors. Table 1 lists the recovery time for some devices from Hamamatsu with quenching resistors of about 150 kOhm. There is no significant dependence of the recovery time on the bias voltage.

Polysilicon resistors are commonly used for quenching the breakdown. These resistors change their value with temperature. Therefore, there is a strong dependence of the recovery time on the temperature. The quenching resistor of a G-APD from Hamamatsu changed from 200 kOhm at room temperature to 1700 kOhm at the temperature of liquid nitrogen [78]. Figure 39 shows the currents as function of the forward bias at different temperatures. The use of a metal alloy with high resistivity like FeCr instead of the polysilicon would be advantageous.

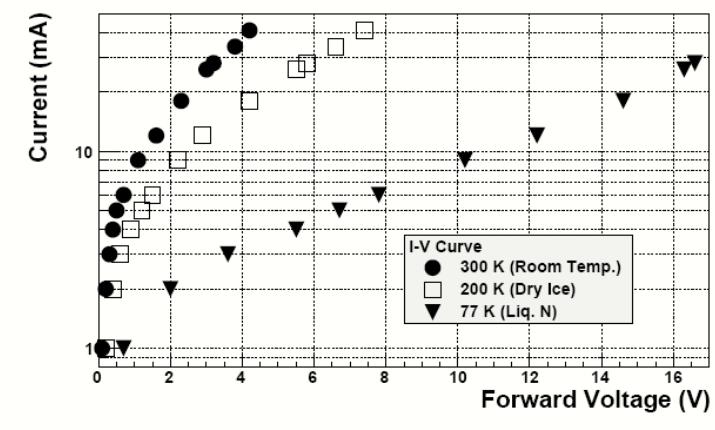

Figure 39. G-APD currents as function of the forward bias measured at different temperatures. The slopes of the curves correspond to the quenching resistance value when the current is sufficiently high. Reprinted from [78].

6.2.9 Pulse shape

The signal rise time is determined by the resistance of the silicon in the breakdown channel, the space charge, the resistance of neutral regions and the parasitic capacitance of the whole device, which is 2 orders of magnitude higher than the capacitance of one single cell. Figure 40 shows the Al lines, which connect all cells to the bias voltage (indicated in green) and form the parasitic capacitance. For a 3×3 mm^2 G-APD with 50×50 μm^2 cells from Hamamatsu, the parasitic capacitance adds up to some 10 pF while the capacitance of a single cell is $\sim$90 fF.

The recharging of the cells defines the signal fall time, which is the same as the recovery time. In some devices, the polysilicon quenching resistor lies on top of the junction area and form a direct capacitive coupling between the resistor itself and the diode. These devices show a short peak with a duration of 2 to 3 ns followed by a slow tail due to the recharging of the cell [79].

When a G-APD is coupled to a scintillating crystal like Lutetium-Yttrium-oxyorthosilicate (LYSO), the rise time of the signals can become quite long (figure 41). This can be explained by a convolution of the G-APD signal fall time with the time distribution of the photon emission of the LYSO scintillation. [80]

This pile-up effect can be minimized by the design of the readout electronics. An amplifier with small input impedance reduces the tail of the signal to a few nanoseconds. Figure 42 shows the response of a G-APD (Hamamatsu S10362-330050C) to a short ($\sim$1 ns) light flash when the G-APD was directly coupled to the 50 Ohm input of an oscilloscope and when an additional 6 Ohm resistor reduced the input impedance to $\sim$5 Ohm. Note that the signal amplitude is also reduced.

6.2.10 Timing

The active layer of silicon in a G-APD is very thin (2 to 4 μm) and the process of the breakdown development is fast. In addition, the signal amplitude is big because of the high cell capacitance. Therefore, very good timing properties even for single photons can be expected. Fluctuations in the avalanche development are mainly due to a lateral spreading by diffusion and by the photons emitted in the avalanche [81, 82]. The vertical avalanche build-up contributes only little to the

2009 JINST 4 P04004

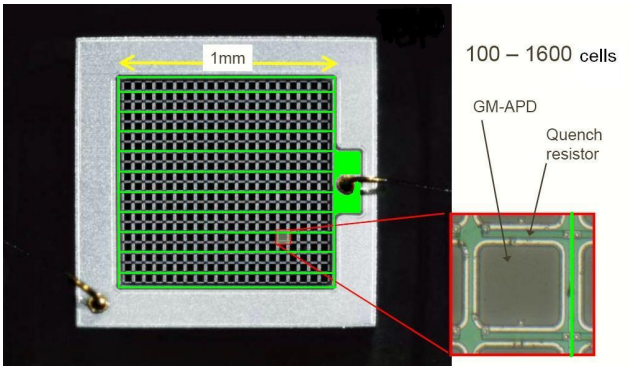

Figure 40. A photo showing the Al lines, which connect all cells to the bias voltage and form an additional parasitic capacitance (indicated in green). Hamamatsu (S10362-33-050C).

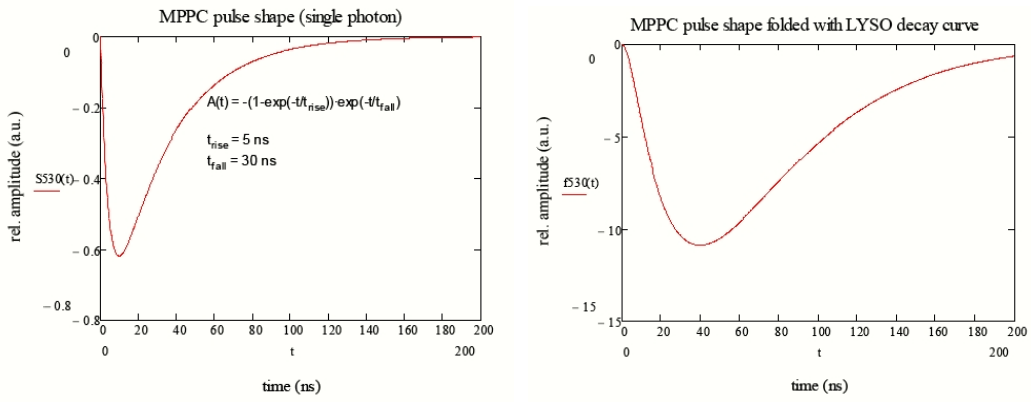

Figure 41. Pulse shape of a G-APD from Hamamatsu (S10362-330050C) for single photons (left) and for photons from a LYSO crystal with a decay time of 40 ns (right). Reprinted from [80].

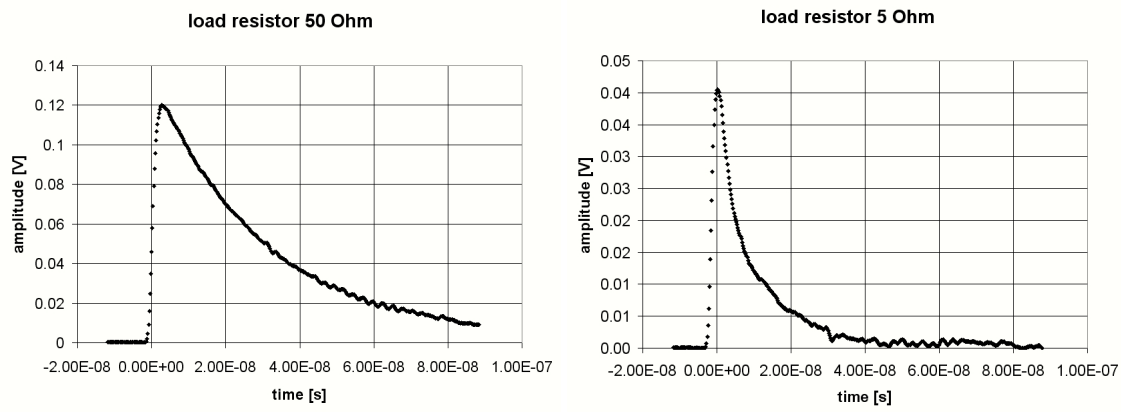

Figure 42. Pulse shape of a G-APD from Hamamatsu (S10362-330050C) when illuminated with 1 ns light flash and coupled to the amplifier of an oscilloscope with 50 Ohm input impedance (left) and 5 Ohm input impedance (right).

2009 JINST 4 P04004

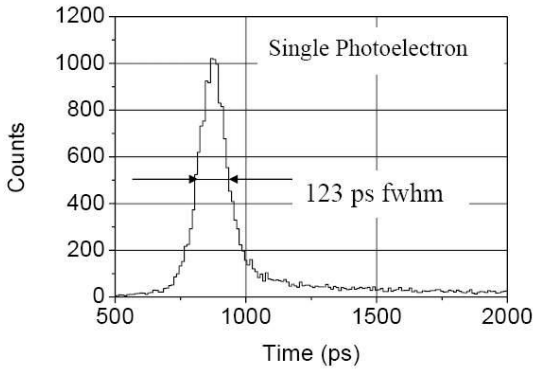

Figure 43. Time resolution for single photons. See text. Reprinted from [45].

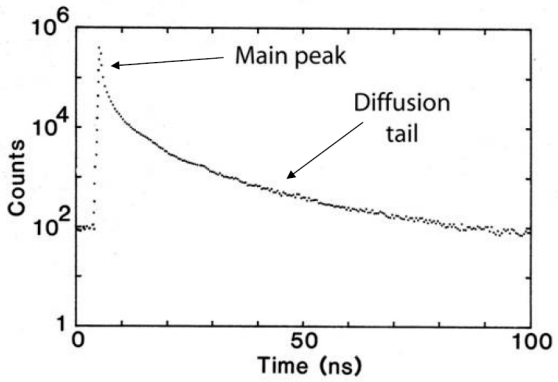

Figure 44. Logarithmic representation of the timing distribution. Reprinted from [71].

timing. Figure 43 shows a measurement of the time response of a G-APD in the case of single photon triggers [45]. The authors state a 40 ps contribution from both the used laser and the electronics. The result, then, is a time resolution with a standard deviation of 42 ps. Operation at high overvoltage (high gain) improves the time resolution.

The tail to the right visible in figure 43 can be explained by carriers created in field-free regions, which have to travel by diffusion [83]. It can take several tens of nanoseconds until they reach a region with field and trigger a breakdown (figure 44). At low gain, the lateral spreading of the depleted volume can be incomplete and can enhance the diffusion tail.

The relative timing of 2 G-APDs (Hamamatsu MPPC-33-050C) coupled to small plastic scintillators (BC422, $4.5 \times 4 \times 2$ mm^3) yielded 50 ps (figure 45). With a single detector, a time resolution of 35 ps RMS can be achieved [84].

6.2.11 Nuclear Counter Effect

Even a heavily ionizing particle traversing a G-APD triggers a breakdown only in the struck cell. The signal looks exactly like the signal produced by a single photon. The nuclear counter effect is therefore negligible.

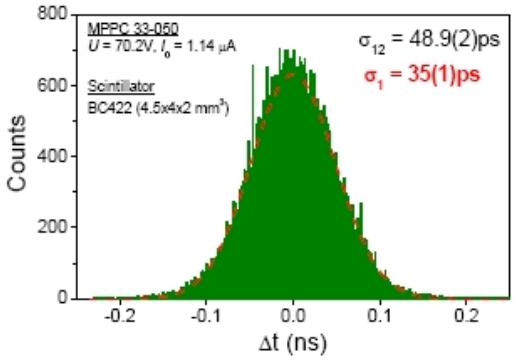

Figure 45. Relative timing of 2 detectors made of G-APDs coupled to plastic scintillators. Reprinted from [84].

6.2.12 Radiation hardness

When G-APDs are used in the harsh radiation environments of high energy physics experiments (such as for the proposed International Linear Collider (ILC) detectors, the CMS detector at LHC, etc.) radiation hardness is a major concern. As has been shown by many investigators, radiation (gammas, electrons, neutrons, charged hadrons, etc.) can produce defects in the silicon bulk or at the Si/SiO_2 interface [85]. Many of these defects are electrically active and can change the doping concentration in the silicon as well as causing charge-trapping effects. As a result, some parameters of G-APDs such as breakdown voltage, leakage current, dark count rate, gain, and photon detection efficiency may change during irradiation.

G-APDs have been irradiated with γ-rays [86], with neutrons [87, 88], with protons [88, 89] and with electrons [90, 91].

The accumulated dose and fluence, respectively, were relatively low compared to the irradiations of PIN diodes and linear APDs with 240 Gy in the case of the γ-ray irradiation by a ^{60}Co source [86], $2.8{\cdot}10^{10}$ protons/cm^2 [88],10^{12} neutrons/cm^2 [87] and $8{\cdot}10^{10}$ electrons/cm^2 [91].

Hadrons create defects in the bulk silicon, which act as generation centers, and the dark current, the dark count rate and the afterpulsing probability will increase during an irradiation. Measurement done with G-APDs from different producers showed significantly increased dark currents and dark counts (figure 46) after irradiation with 10^{10} protons/cm^2 [89]. Normalized to an irradiation with 1 MeV neutrons, which is the standard in irradiation studies, the accumulated proton fluence is equivalent to an irradiation with $2{\cdot}10^{10}$ neutrons/cm^2.

No change, which is not compatible with the measurement errors, has been reported for the PDE, the breakdown voltage, the crosstalk probability and the value of the quenching resistors. Only devices with a high value of the quenching resistor showed a reduction of the signal amplitude when they are operated at high gain. This can be explained by the long recovery time of these devices in combination with the high dark count rates. Quite a few cells are in a recovery phase when the test light flashes impinge. They are therefore not fully recharged and the signals amplitude is reduced and, in addition, the trigger probability is lower.

The defects are produced in the full volume of the G-APDs. Therefore, the argument used in the discussion of the thermally generated dark counts holds and devices produced on an n-type

2009 JINST 4 P04004

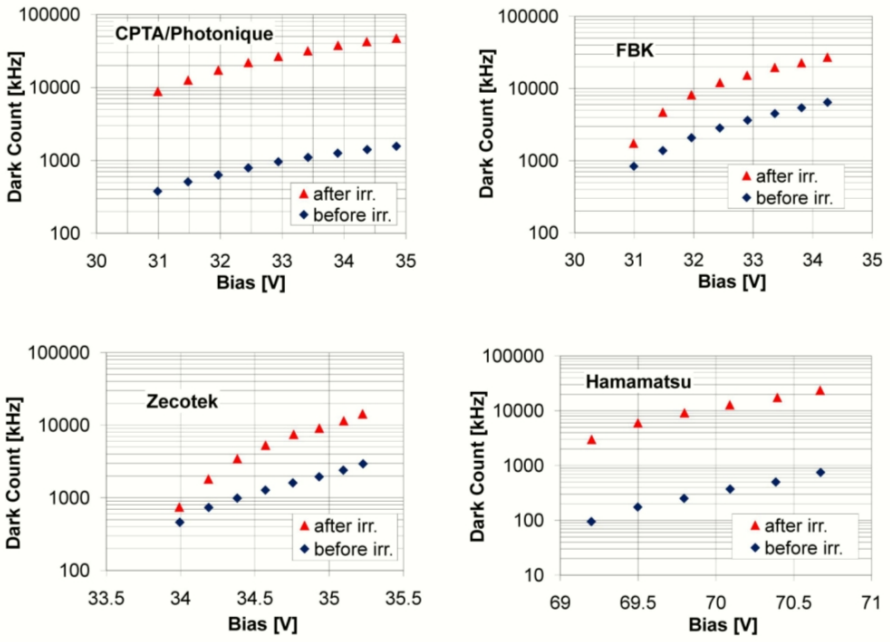

Figure 46. Dark counts vs. bias voltage of G-APDs from 4 producers, measured before and after proton irradiation. Reprinted from [89].

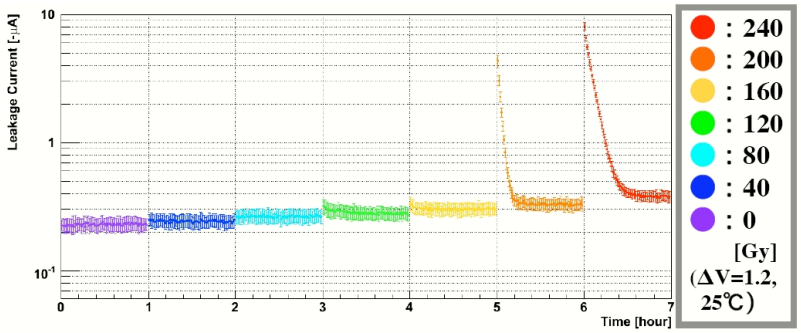

Figure 47. Dark currents measured after 6 irradiations with a dose of 40 Gy each. Figure from [86].

substrate potentially perform better under irradiation. The thickness of the p-layer is normally much thinner than in a n-on-p type G-APD and less electrons with their high trigger probability in comparison to the probability of holes will drift towards the p-n junction.

An irradiation with γ-rays from a ^{60}Co source causes defects in the bulk only with very low probability but there is a serious effect on the surface at the Si/SiO_2 interface. When, after the irradiation, a G-APD from Hamamatsu (T2K-11-100C) was biased, it developed high dark currents and produced large dark counts with an amplitude corresponding to a signal of more than 10 photo electrons. After a couple of minutes, all signals with large amplitudes and most of the dark current disappeared (figure 47). This phenomenon reappeared when the bias voltage was turned off and, after a while, turned on again [86].

With an infrared sensitive camera the regions, where the high current was flowing, have been

2009 JINST 4 P04004

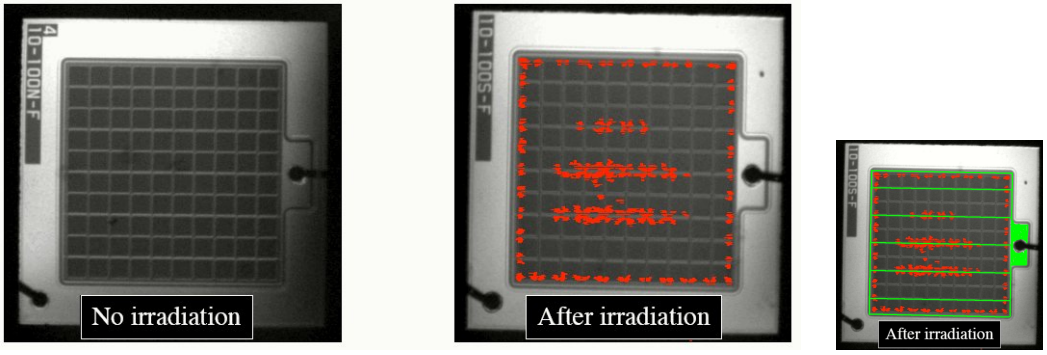

Figure 48. Picture of a G-APD taken with an infrared camera before and after irradiation with a dose of 240 Gy from a ^{60}Co source. The small picture to the right indicates in green the areas, which are covered by aluminum lines (reprinted from [86]).

localized. The outer edge of the device near the Al lines and regions along the bias lines connecting all the cells could be identified as sources (figure 48). Very likely the effect was caused by accumulated and stationary charges at the surface generated by the breakup of SiO_2 molecules. An irradiation of the same type of G-APD (and devices from other producers) with twice the dose, with 500 Gy from a ^{60}Co source, has been carried out at PSI. No such effect has been observed. The reason might be that the irradiation at PSI had been done without applied bias voltage.

A similar effect was observed in prototypes during the development of the linear APDs for CMS [92]. With a proper design of the width of the isolation on the surface, the sensitivity to γ-radiation could be eliminated.

6.2.13 Long term stability

The failure rate of the G-APDs is an important figure of merit. An exposure to elevated temperature, the so-called accelerated aging, can be used to study the expected life-time of semiconductor devices. At INR (Moscow) 19 G-APDs from CPTA have been placed in an oven at 80 °C for 30 days. All photodiodes were kept under bias voltage to provide the same dark current as in working mode at room temperature. Only one G-APD, the one with the lowest PDE, failed the temperature test. All other devices passed the test without residual effects. The signals of the tested photodiodes in response to an LED light were measured before heating and for a period of about 260 days after heating. The devices were stored without bias in between the control measurements. The stability of the light source over time was monitored with a few reference photosensors.

The results for two devices are presented in figure 49. The accuracy of these measurements is about $\pm$2.0 p.e. due to a misalignment between the light aperture and the sensitive area of the tested MRS photodiodes. No degradation in the light signal was observed for more than 7 months after the heat treatment [93]

6.2.14 More features of G-APDs

- G-APDs work at low bias voltage ($<$100 V)
- have low power consumption ($<$ 50 μW/mm^2),

2009 JINST 4 P04004

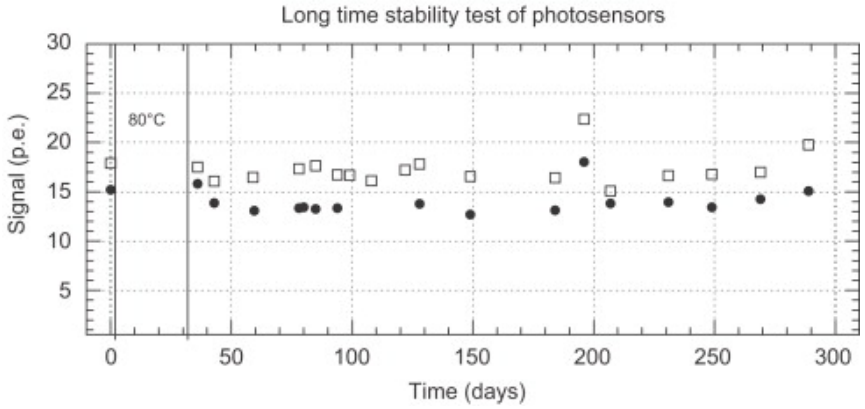

Figure 49. Light yields of two G-APDs measured with a green LED before and after a heating test. Each point has an error of ± 2.0 photo-electrons. Reprinted from [93].

Figure 50. Photograph of an 8 inch wafer with G-APDs produced by Zecotek Photonics Inc. before dicing.

- are insensitive to magnetic fields (tested up to 7 T, but operation at much higher fields can be expected),
- are compact and rugged,
- tolerate accidental illumination
- have the potential for low-cost mass production

These attributes make G-APDs superior to PMTs in many applications. The main drawbacks are:

- The small area presently available. The largest device currently produced has an area of 25 mm^2. Unless there is a significant improvement of the design and the production process,

2009 JINST 4 P04004

which results in a reduction of the dark count rate and in parasitic capacitance, the area cannot exceed few cm^2,

- the strong correlation of the PDE to the overvoltage and by this to the relative gain of the device,
- the high noise rate per unit area,
- the high sensitivity of the gain of most devices to temperature and voltage changes.
- an increase of the signal rise time due to the large parasitic capacitance of large area G-APDs.

6.2.15 Choice of parameters

As already mentioned, many different designs are possible and G-APDs can be quite well tailored to specific needs of experiments. The number of design and performance parameter variations is much larger than that of a PMT or a normal linear APD. Compared to the still mostly hand-made PMTs, the G-APDs are much more suited for mass production methods although many different masks, multiple production steps and special tooling are required. Therefore, any change of the G-APD configuration will be much more costly compared to a PMT configuration change. In the following list, a number of design choices are given together with the consequences on some operating parameters:

- Semiconductor material — has influence on the PDE and the range of sensitivity as a function of wavelengths
- p-silicon on a n-substrate — highest detection efficiency for blue light
- n-silicon on a p-substrate — highest detection efficiency for green light
- Thickness of the depleted layers — range of wavelengths, gain, optical crosstalk, dark counts
- Doping concentrations — operating voltage and its range
- Impurities and crystal defects — dark counts, afterpulses
- Area of the cells — gain, geometric factor, dynamic range, recovery time
- Value of the quenching resistors — recovery time, count rate/cell
- Type of resistors — temperature dependence
- Optical cell isolation (groove) — crosstalk

Many applications need the highest possible photon detection efficiency but do not need a large dynamic range (RICH, DIRC, IACT, EUSO, photon correlation studies, fluorescence spectroscopy, single electron LIDAR, neutrino detectors). For nearly all of these applications, a G-APD with p-on-n structure, large cells (50 to 100 μm^2), small value of the individual resistors and maybe optical isolation between the cells is best suited.

Other applications need a large dynamic range (HEP calorimeters, PET, SPECT, scintillator readout, Smart PMTs,[4] radiation monitors). In most cases, a p-on-n structure again with small cells (5 to 30 μm^2) is best. An optical isolation is not necessary.

Some applications like a tile calorimeter with wavelength shifting fibers are better off with a n-on-p structure because the wavelength shifting principle is based on the principle that the light of the source element is shifted to longer wavelengths, i.e. more to the redder part of the spectrum.

7 Some applications of solid state photo sensors in particle physics and related fields

The following list of applications is meant to give only a short overview and is far from being complete — we apologize that many excellent instruments could not be mentioned.

As already mentioned, large area (a few cm^2) PIN photo diodes are successfully used in many big and numerous small experiments, mostly in high energy physics.

APDs are for the first time being used in large quantity in the electromagnetic calorimeter of the CMS detector at LHC [36]. The Panda experiment at FAIR, Darmstadt, plans the utilization of APDs with a larger area (1 cm^2) for the readout of the $PbWO_4$ crystals in the calorimeter [94]. In smaller experiments, APDs have been successfully used for years (see, for example, [95]). An excellent energy resolution has been obtained in the detection of X-rays with energies of several hundred keV [96]. A first PET scanner with APD readout has been constructed [97]. A scanner for brain investigations of small animals has been built and is operated with very good results [98]. More PET instruments have followed (see e.g. [99]). Recently, a combination of PET and MRI, which together provides information about metabolism and functionality with very good anatomical information, has been assembled and is under test [100]. Also being investigated is a combination of PET and CT [101].

Direct detection of X-rays with energies from 2 to 20 keV with so-called reach through APDs has become a standard tool at synchrotron radiation facilities [102].

G-APDs are relatively new devices and, therefore, most detectors with G-APDs are prototypes. Most advanced is the so-called near neutrino detector of the Tokai-to-Kamioka experiment with some 60000 G-APDs. Plastic scintillators with various shapes have wavelength shifting fibers in holes or grooves and the G-APDs are mounted on one or on both ends of the fibers [103]. The installation will start in January 2009 and data-taking is foreseen in the same year. A similar concept with plastic scintillator, wavelength shifting fibers and G-APD readout is planned for the ILC and large-scale prototypes have been realized and tested [104–106].

For an upgrade of the Belle detector at the KEK B-factory, a proximity focusing ring image Cherenkov counter (RICH counter) has been proposed [107]. It has been demonstrated that G-APDs are promising as detectors of Cherenkov photons inside large magnetic spectrometers.

In solid-state physics with the muon spin rotation technique (MuSR), which needs high magnetic fields, the replacement of PMTs by G-APDs has made the experimental setup less complicated and more efficient [84].

A new design of a PET instrument, which avoids the parallax error caused by the normally unknown depth of interaction, the so-called AxPET, became possible by the use of G-APDs [108].

[4] In a Smart PMT the electrons liberated by a photon in a photocathode are accelerated and focused on a scintillating crystal. The scintillation light is then detected by a PMT or a solid state photo sensor.

2009 JINST 4 P04004

A demonstrator is currently being assembled. Developed and tested is a PET block detector based on G-APDs. The results are very promising [109]. In PET-MRI combinations, the G-APDs offer a big advantage because of their compactness, high internal gain and insensitivity against electromagnetic interference (EMI). Normal linear APDs have only moderate internal gain and need low noise amplifiers, which have to be limited in bandwidth for noise suppression and have to be carefully shielded in a PET-MRI system. The shielding can have significant influence on the MRI image quality.

It has been shown that Cherenkov light produced in air showers, which are initiated by high energetic cosmic rays, can be detected by G-APDs with high sensitivity [110]. A full-sized prototype camera for an imaging air shower Cherenkov telescope with G-APDs (instead of the traditional PMTs) is currently under construction [111]. Assuming that the predicted high PDE can be reached, an improvement in sensitivity by a factor 2-3 is expected compared with classical PMTs.

A detector for time resolved X-ray photon correlation spectroscopy (XPCS) with 64 APDs operated in Geiger-mode has been built and first experiments were performed [112].

The possible applications in chemistry and biology wherever fluorescence analysis is needed are numerous.

8 Prospects for G-APDs made from other semiconductors

Currently, silicon is the by far best understood and by far the most frequently used semiconductor material. Therefore, it is not surprising that nearly all manufactured types of large area PIN photodiodes, APDs and G-APDs are based on silicon. There exist many other semiconductor materials, which are nowadays pursued for alternative applications, mainly on III-V materials. Most of the activities concentrate on developments for LEDs, laser diodes and microwave components. Industry is steadily improving the purification of these materials and the growth of high quality, cost effective crystals. It will, therefore, only be a question of time before G-APDs based on materials other than silicon will be fabricated. The main reasons are the prospects of producing G-APDs with lower noise and possibly higher sensitivity in the UV and blue spectral region. The reduction of noise is strongly correlated with a higher bandgap material and high purity materials, which also should have few lattice defects. One can even list a number of requirements in the search for useful semiconductor candidates:

- A bandgap wider than that of silicon.
- High purity intrinsic materials.
- Ability to grow crystals with few lattice defects.
- Suitable doping materials for both n and p structures.
- A sufficiently large lifetime of the carriers.
- Holes must also contribute to electron-hole pair production to start secondary avalanches.
- A key requirement is that the production of secondary photons in the avalanche process should be very small, i.e. it must be an indirect bandgap material.

2009 JINST 4 P04004

- The mobility of both the electrons and holes should be high.
- It should be possible to passivate the surface easily.
- The refractive index of the semiconductor should be not too large (or else large surface reflectivity losses occur).

Basically all materials that are well suited for LED or laser diode fabrication can already be excluded.

9 Conclusions and outlook

After nearly three decades of intense developments in semiconductor photo sensors, it was possible to produce silicon-based detectors of suitable area and power to detect single photons. This was mostly independent of developments for very small area photo detectors, which were driven by the needs in the communication sector, whereas the developments described here were initially driven by the needs for high energy physics experiments and proceeded basically in three steps: at first, the development of low-noise PIN photo diodes, then of large area, linear-mode APDs and finally of multi-cell G-APDs. The latter development is still ongoing, partly because of the complexity of parameter options and partly because optimizations have not yet reached a high enough level of maturity. In the area of PIN photodiodes and APDs, basically all fundamental problems and limitations are well understood and progress is mostly expected in producing larger area detectors. The development for industrial production of PIN photo diodes and APDs took about 8 years and has now reached a production price level of $<1\$/mm^2$ sensitive area. The prices per mm^2 are still exceeding by a significant factor that of the price per unit area of PMTs but for many applications not demanding single photon sensitivity other factors like compactness, insensitivity to magnetic fields, low operation voltage or finer pixel structures justify the higher price per unit area for PIN photodiodes and APDs.

It is expected that a similar time-span of around 8 years is needed for the large scale industrial production of G-APDs, i.e. still a few more years are needed to reach the same high level of maturity. There are still quite a few challenges awaiting both a better understanding of the fundamental processes in the avalanche process and noise generation as well as improvements in the production techniques in order to lower the price below $1\$/mm^2$, which is eventually needed to compete with small area PMTs. The following matter await solutions:

- Reduction in noise and optical cross-talk, the latter condition without increasing the dead area between cells.
- Reduction in gain for relatively large cell sizes (volumes), alternatively developments for ultra-narrow grooves between cells for the suppression of optical cross-talk.
- Increase in area without spoiling fast signals, respectively without an increase in the parasitic capacitance for large area G-APDs.
- Replacement of the amorphous silicon quenching resistor by a resistor of low temperature coefficient, for example by FeCr resistors.

2009 JINST 4 P04004

- Enhancement of the UV sensitivity by ultra-thin p++ top layers.
- Improving/optimization of the recovery time of fired cells.
- Better measurements/understanding of some fundamental parameters such as tunneling or field emission, production of noise electrons, the effect of generation/recombination centers in the semiconductors influencing afterpulses and noise, the voltage limit that quenches the avalanches (must be slightly below the normal breakdown voltage), the complete spectrum of the photon production in avalanches and their contribution to secondary avalanches.
- More realistic and improved programs for better simulation of the performance taking electrons, holes and secondary photons and their dynamics properly into account.
- A better understanding of the PDE as a function of voltage and temperature changes.
- Production processes to increase the radiation hardness.
- Solutions have to be found for when a very high dynamic range is needed, as in calorimeters and in digital CT.

Nevertheless, for quite a few applications G-APDs can already now be used. In most cases, either the requirement for small photo sensors or the insensitivity to magnetic fields was more important than a high stability or a very high PDE. One particularly noticeable area is the light sensor development for PET detectors and especially for PET-MRI detectors where very likely the G-APD will completely dominate the market, provided that their price drops.

Finally, we want to add a few comments not entirely related to the open questions listed above.

- For the time being, the needs for large area light detectors with single photon response can only be fulfilled by large area PMTs.
- In the important area of small element multi-pixel arrays with single photon sensitivity the PMTs can already now no longer compete with G-APDs except in a few specific applications (high temperature, low noise)
- The technology to produce G-APDs is very similar to the technology to produce integrated electronics. This opens entirely new configurations to integrate G-APDs for single photon detection with various electronics circuits, such as amplifiers, comparators, ADCs and logic elements etc. on the same silicon chip. Such combinations are completely impossible to achieve with PMTs and very difficult to achieve with PIN photodiodes or APDs because of the very different production techniques.

Acknowledgments

We would like to thank many of our colleagues working on studies of PIN photodiodes, APDs and G-APDs for many useful discussions, comments and provision of some of the data. In particular, we thank Boris Dolgoschein, Victor Golovin, Anton Kabelschacht, Yuri Kudenko, Rasmik Mirzoyan, Yuri Musienko, Rainer Richter, Zair Sadygov and Alexey Stoykov. Also, we are grateful to the numerous companies, which have sent us prototypes of different detector models.

2009 JINST 4 P04004

References

[1] R.S. Ohl, *Light-Sensitive Electric Device*, U.S. Patent 2402662, filed May 27, 1941, Issued June 25, 1946.

[2] M. Lesser, *Antireflection coatings for silicon charge-coupled devices*, *Optic. Eng.* **26** (1987) 911.

[3] K. Rajkanan, R.Singh and J. Shewchun, *Absorption coefficient of silicon for solar cell calculations*, *Solid-State Electron.* **22** (1979) 793.

[4] E.J. Ryder, *Mobility of holes and electrons in high electric fields*, *Phys. Rev.* **90** (1953) 766.

[5] P. Fischer, *An Area efficient 128-channel counter chip*, *Nucl. Instrum. Meth.* **A 378** (1996) 297.

[6] R. Ballabriga et al., *The Medipix3 prototype, a pixel readout chip working in single photon counting mode with improved spectrometric performance*, *IEEE Trans. Nucl. Sci.* **54** (2007) 1824.

[7] M. Locker et al., *Single photon counting X-ray imaging with Si and CdTe single chip pixel detectors and multichip pixel modules*, *IEEE Trans. Nucl. Sci.* **51** (2004) 1717.

[8] C. Broennimann et al., *The PILATUS 1M detector*, *J. Synchroton Rad.* **13** (2006) 120.

[9] A. Bergamaschi et al., *Experience and results from the 6 Megapixel Pilatus System*, PoS(Vertex2007)049.

[10] K. Yamamoto et al., *Highly stable silicon pin photodiode*, *Nucl. Instrum. Meth.* **A 253** (1987) 542.

[11] H. Grassmann, E. Lorenz, H.G. Moser and H. Vogel, *Results from a CsI(Tl) test calorimeter with photodiode readout between 1-GeV AND 20-GeV*, *Nucl. Instr. Meth.* **A235** (1985) 319;
E. Lorenz, *Scintillation calorimetry and readout techniques*, *IEEE Trans. Nucl. Sci.* **31** (1984) 48.

[12] L3 collaboration, J.A. Bakken et. al., *Performance of a prototype BGO calorimeter in an electron beam from 2-GeV TO 50-GeV*, *Nucl. Instr. Meth.* **A 254** (1987) 535.

[13] C. Bebek, *A cesium iodide calorimeter with photodiode readout for CLEO-II*, *Nucl. Instrum. Meth.* **A 265** (1988) 258.

[14] CRYSTAL BARREL collaboration, E. Aker et. al., *The Crystal Barrel spectrometer at LEAR*, *Nucl. Instrum. Meth.* **A 321** (1992) 69.

[15] A. Abashian et al., *The Belle detector*, *Nucl. Instrum. Meth.* **A 479** (2002) 117.

[16] BABAR collaboration, B. Aubert et. al., *The BaBar detector*, *Nucl. Instrum. Meth.* **A 479** (2002) 1.

[17] D. Bédérède et al., *Performances of the CsI(Tl) detector element of the GLAST calorimeter*, *Nucl. Instrum. Meth.* **A 518** (2004) 15.

[18] Hamamatsu S8550, datasheet, http://sales.hamamatsu.com/assets/pdf/parts_S/S3590-18_-19.pdf.

[19] V. Radeka, *Semiconductor detectors and readout electronics: present directions and outstanding problems*, *Nucl. Instrum. Meth.* **A 253** (1987) 309.

[20] P. Lechner et al., *Silicon drift detectors for high resolution room temperature X-ray spectroscopy*, *Nucl. Instrum. Meth.* **A 377** (1996) 346.

[21] C. Fiorini et al., *Gamma-ray spectroscopy with $LaBr_3$:Ce scintillator readout by a silicon drift detector*, *IEEE Trans. Nucl. Sci.* **53** (2006) 2392.

[22] M. Moszynski et al., *A comparative study of silicon drift detectors with photomultipliers, avalanche photodiodes and PIN photodiodes in gamma spectroscopy with $LaBr_3$ crystals*, submitted to IEEE Trans. Nucl. Sci.

2009 JINST 4 P04004

[23] R. Wunstorf et al., *Damage-induced surface effects in silicon detectors*, Nucl. Instrum. Meth. **A 377** (1996) 290.

[24] A. Vasilescu and G. Lindstroem, *Displacement damage in silicon*, on-line compilation, http://sesam.desy.de/members/gunnar/Si-dfuncs.html.

[25] SICAPO collaboration, M. Bosetti et. al., *Effect on charge collection and structure of n type silicon detectors irradiated with large fluences of fast neutrons*, Nucl. Instrum. Meth. **A 343** (1994) 435.

[26] R.J. McIntyre, *A new look at impact ionization-Part I: A theory of gain, noise, breakdown probability, and frequency response*, IEEE Trans. Electron. Dev. **46** (1999) 1623.

[27] C.A. Lee et al., *Ionization Rates of Holes and Electrons in Silicon*, Phys. Rev. **134** (1964) A761.

[28] P.P. Webb, R.J. McIntyre and J. Conradi, *Properties of avalanche photodiodes*, *RCA Review* **35** (1974) 234.

[29] M. Moszynski et al., *Large area avalanche photodiodes in X-rays and scintillation detection*, Nucl. Instrum. Meth. **A 442** (2000) 230.

[30] C.P. Allier et al., *Readout of a $LaCl_3(Ce^{3+})$ scintillation crystal with a large area avalanche photodiode*, Nucl. Instrum. Meth. **A 485** (2002) 547.

[31] R. Chandrasekharan, M. Messina and A. Rubbia, *Detection of VUV light at high quantum efficiency with large area avalanche photodiodes (LAAPDs)*, Nucl. Instrum. Meth. **A 567** (2006) 45.

[32] J. Kataoka et. al., *Recent progress of avalanche photodiodes in high-resolution X-rays and Gamma-rays detection*, Nucl. Instrum. Meth. **A 541** (2005) 398.

[33] K. Deiters et. al., *Properties of the most recent avalanche photodiodes for the CMS electromagnetic calorimeter*, Nucl. Instrum. Meth. **A 442** (2000) 193.

[34] T. Kirn et. al., *Wavelength dependence of avalanche photodiode (APD) parameters*, Nucl. Instrum. Meth. **A 387** (1997) 202.

[35] R.J. McIntyre, *The distribution of gains in uniformly multiplying avalanche photodiodes: Theory*, *IEEE Trans. Nucl. Sci.* **19** (1972) 703.

[36] K. Deiters et. al., *Investigation of the avalanche photodiodes for the CMS electromagnetic calorimeter operated at high gain*, Nucl. Instrum. Meth. **A 461** (2001) 574.

[37] D. Renker, *Properties of avalanche photodiodes for applications in high energy physics, astrophysics and medical imaging*, Nucl. Instrum. Meth. **A 486** (2002) 164.

[38] V. Radeka, *Optimum Signal-Processing for Pulse Amplitude Spectrometry in the Presence of High-Rate Effects and Noise*, IEEE Trans. Nucl. Sci. **15** (1968) 455.

[39] S. Baccaro et. al., *Radiation damage effect on avalanche photodiodes*, Nucl. Instrum. Meth. **A 426** (1999) 206.

[40] K. Deiters et. al., *Double screening tests of the CMS ECAL avalanche photodiodes*, Nucl. Instrum. Meth. **A 543** (2005) 549.

[41] Hamamatsu S8550, datasheet, http://sales.hamamatsu.com/assets/pdf/parts_S/S8550.pdf.

[42] http://www.rmdinc.com/products/p006.html.

[43] A. Bross et. al., *Characterization and performance of visible light photon counters (VLPCs) for the upgraded D0 detector at the Fermilab Tevatron*, Nucl. Instrum. Meth. **A 477** (2002) 172.

[44] D0 collaboration, S. Abachi et. al., *The D0 Detector*, Nucl. Instrum. Meth. **A 338** (1994) 185.

2009 JINST 4 P04004

[45] P. Buzhan et. al., *Silicon photomultiplier and its possible applications*, *Nucl. Instrum. Meth.* **A 504** (2003) 48.

[46] R.J. McIntyre, *Theory of microplasma instability in silicon*, *J. Appl. Phys.* **32** (1961) 983.

[47] R.H. Haitz., *Model for the electrical behavior of a microplasma*, *J. Appl. Phys.* **35** (1964) 1370.

[48] http://optoelectronics.perkinelmer.com/content/ApplicationNotes/APP_APDUsersGuide.pdf.

[49] F. Zappa et al., *Fully-integrated active-quenching circuit for single-photon detection*, *Proc. of the 28th European Solid-State Circuits Conference*, ESSCIRC 2002, pg. 355.

[50] S. Vasile et al., *High gain avalanche photodiode arrays for DIRC applications*, *IEEE Trans. Nucl. Sci.* **46** (1999) 848.

[51] P.P. Antich et al., *Avalanche photo diode with local negative feedback sensitive to UV, blue and green light*, *Nucl. Instrum. Meth.* **A 389** (1997) 491.

[52] V. Saveliev and V. Golovin, *Silicon avalanche photodiodes on the base of metal-resistor-semiconductor (MRS) structures*, *Nucl. Instrum. Meth.* **A 442** (2000) 223.

[53] V. Golovin, *Avalanche Photodetector*, Russian Agency for Patents and Trademarks, Patent No. RU 2142175 (1998).

[54] Z. Sadygov, *Avalamche Detector*, Russian Agency for Patents and Trademarks, Patent No. RU 2102820 (1998).

[55] Z. Sadygov et al., *Three advanced designs of micro-pixel avalanche photodiodes: Their present status, maximum possibilities and limitations*, *Nucl. Instrum. Meth.* **A 567** (2006) 70.

[56] D.E. Groom, *Silicon photodiode detection of bismuth germanate scintillation light*, *Nucl. Instrum. Meth.* **219** (1984) 141.

[57] V. Andreev et. al., *A high granularity scintillator hadronic-calorimeter with SiPM readout for a linear collider detector*, *Nucl. Instrum. Meth.* **A 540** (2005) 368.

[58] Y. Musienko et al., *Tests and performance of multipixel Geiger mode APD'*, PoS(PD07)012.

[59] W.G. Oldham et al., *Triggering phenomena in avalanche diodes*, *IEEE Trans. Electron. Dev.* **19** (1972) 1056.

[60] R.J. McIntyre, *On the avalanche initiation probability of avalanche diodes above the breakdown voltage*, *IEEE Trans. Electron. Dev.* **20** (1973) 637.

[61] http://www.photonique.ch/Prod_0710G9MM.html.

[62] G.A.M. Hurkx et al., *A new recombination model for device simulation including tunneling* , *IEEE Trans. Electron. Dev.* **39** (1992) 331.

[63] G.A.M. Hurkx et al., *A new analytical diode model including tunneling and avalanche breakdown*, *IEEE Trans. Electron. Dev.* **39** (1992) 2090.

[64] A. Lacaita et al., *On the bremsstrahlung origin of hot-carrier-induced photons in silicon devices*, *IEEE Trans. Electron. Dev.* **40** (1993) 577.

[65] N. Otte, *On the efficiency of photon emission during electrical breakdown in silicon*, NDIP08, to be published in Nucl. Instrum. Meth. A.

[66] J. Bude and K. Hess, *Impact ionization in semiconductors: Effects of high electric fields and high scattering rates*, *Phys. Rev.* **B 45** (1992) 10958.

2009 JINST 4 P04004

[67] J.H. Swoger and S.J. Kovacic, *Enhanced luminescence due to impact ionization in photodiodes*, *J. Appl. Phys.* **74** (1993) 2565.

[68] A. Lacaita et al., *Recent advances in the detection of optical photons with silicon photodiodes*, *Nucl. Instrum. Meth.* **A 326** (1993) 290.

[69] S. Villa, A.L. Lacaita and A. Pacelli, *Photon emission from hot electrons in silicon*, *Phys. Rev.* **B 52** (1995) 10993.

[70] N. Akil et al., *A multimechanism model for photon generation by silicon junctions in avalanche breakdown*, *IEEE Trans. Electron. Dev.* **46** (1999) 1022.

[71] Cova et al., *Evolution and prospect of single-photon avalanche diodes and quenching circuits*, *J. Modern Opt.* **51** (2004) 1267.

[72] N. Basharuli et al., *Registration of charged particles by scintillating fibers coupled with micro-cell Si APD*, Advanced Technology and Particle Physics, World Scientific, Singapore (2002), p. 627.

[73] P. Buzhan et al., *Large area silicon photomultipliers: performance and applications*, *Nucl. Instrum. Meth.* **A 567** (2006) 78.

[74] W.J. Kindt, *Geiger Mode Avalanche Photodiode Arrays*, Thesis, Delft University Press (1999).

[75] S. Korpar et. al., *Measurements of Cherenkov photons with silicon photomultipliers*, arXiv:0812.0531.

[76] Th. Kraehenbuehl, *G-APD arrays and their use in axial PET modules*, Diploma thesis, ETH Zuerich (2008).

[77] H. Oide et al., *Study of afterpulsing of MPPC with waveform analysis*, PoS(PD07)008.

[78] H. Otono et al., *Study of MPPC at liquid nitrogen temperature*, PoS(PD07)007.

[79] C. Piemonte et al., *Characterization of the first prototypes of silicon photomultiplier fabricated at ITC-irst*, *IEEE Trans. Nucl. Sci.* **54** (2007) 236.

[80] Ch. Casella et al., *Readout of a LYSO crystal with MPPCs. Calculations and measurements of the signal shape*, AX-PET note 2008-001.

[81] A. Lacaita et al., *Observation of avalanche propagation by multiplication assisted diffusion in p-n junctions*, *Appl. Phys. Lett.* **57** (1990) 489.

[82] A. Lacaita et al., *Photon-assisted avalanche spreading in reach-through photodiodes*, *Appl. Phys. Lett.* **62** (1993) 606.

[83] F. Zappa et al., *Principles and features of single-photon avalanche diode arrays*, *Sensor. Actuators* **A 140** (2007) 103.

[84] A. Stoykov et al., *First experience with G-APDs in μSR instrumentation*, NDIP08, to be published in Nucl. Instrum. Meth. A.

[85] G. Lutz, *Semiconductor radiation detectors*, Springer Verlag, Berlin (1999).

[86] T. Matsubara et al., *Radiation damage of MPPC by gamma-ray irradiation with Co 60*, PoS(PD07)032.

[87] I. Nakamura, *Radiation Damage of Pixelated Photon Detector by Neutron Irradiation*, NDIP08, to be published in Nucl. Instrum. Meth. A.

[88] T. Matsumura et al., *Radiation damage to MPPCs by irradiation with protons*, PoS(PD07)033.

2009 JINST 4 P04004

[89] Y. Musienko et al., *Study of radiation damage induced by 82 MeV protons on multi-pixel Geigermode avalanche photodiodes*, NDIP08, to be published in Nucl. Instrum. Meth. A.

[90] S. Sanchez Majos, P. Achenbach and J. Pochodzalla, *Characterisation of radiation damage in silicon photomultipliers with a Monte Carlo model*, *Nucl. Instrum. Meth.* **A 594** (2008) 351.

[91] Y. Musienko et. al., *Radiation damage studies of multipixel Geiger-mode avalanche photodiodes*, *Nucl. Instrum. Meth.* **A 581** (2007) 433.

[92] J. Grahl et. al., *Radiation hard avalanche photodiodes for CMS ECAL*, *Nucl. Instrum. Meth.* **A 504** (2003) 44.

[93] O. Mineev et. al., *Scintillator counters with multi-pixel avalanche photodiode readout for the ND280 detector of the T2K experiment*, *Nucl. Instrum. Meth.* **A 577** (2007) 540.

[94] PANDA collaboration, B. Lewandowski, *A fast and compact electromagnetic calorimeter for the PANDA detector at GSI*, *Nucl. Instrum. Meth.* **A 537** (2005) 349.

[95] H. Nishguchi, *The MEG positron spectrometer*, *Nucl. Instrum. Meth.* **A 581** (2007) 538.

[96] M. Moszynski et al., *Large area avalanche photodiodes in scintillation and X-rays detection*, *Nucl. Instrum. Meth.* **A 485** (2002) 504.

[97] R. Lecomte et al., *Initial results from the Sherbrooke avalanche photodiode positron tomograph*, *IEEE Trans. Nucl. Sci.* **43** (1996) 1952.

[98] C. Woody et al., *RatCAP: a small, head-mounted PET tomograph for imaging the brain of an awake RAT*, *Nucl. Instrum. Meth.* **A 527** (2004) 166.

[99] S. Ziegler et al., *A prototype high-resolution animal positron tomograph with avalanche photodiode arrays and LSO crystals*, *Eur. J. Nucl. Med. Mol. I.* **28** (2001) 136.

[100] B. Pichler et al., *Positron emission tomography/magnetic resonance imaging: the next generation of multimodality imaging?*, *Semin. Nucl. Med.* **38** (2008) 199.

[101] Ph. Berard et al., *Investigation of the LabPET^{TM} detector and electronics for photon-counting CT imaging*, *Nucl. Instrum. Meth.* **A 571** (2007) 114.

[102] J. Kataoka et. al., *Recent progress of avalanche photodiodes in high- resolution X-rays and Gamma-rays detection*, *Nucl. Instrum. Meth.* **A 541** (2005) 398.

[103] Y. Kudenko, *The near neutrino detector for the T2K experiment*, *Nucl. Instrum. Meth.* **A 598** (2009) 289.

[104] V. Andreev et. al., *A high granularity scintillator hadronic-calorimeter with SiPM readout for a linear collider detector*, *Nucl. Instrum. Meth.* **A 540** (2005) 368.

[105] M. Danilov and G. Eigen, *The calice analog scintillator-tile hadronic calorimeter prototype*, SNIC-2006-0211 (2006).

[106] S. Itoh et. al., *Performance of a shower maximum detector with avalanche photodiode readout*, *Nucl. Instrum. Meth.* **A 589** (2008) 370.

[107] S. Korpar et. al., *Silicon photomultiplier as a detector of Cherenkov photons*, *Nucl. Instrum. Meth.* **A595** (2008) 161.

[108] A. Braem et al., *Wavelength shifter strips and G-APD arrays for the read-out of the z-coordinate in axial PET modules*, *Nucl. Instrum. Meth.* **A 586** (2008) 300.

[109] A. Kolb et al., *PET block detector readout approaches using G-APDs*, IEEE NSS-MIC Dresden 2008, to be published in IEEE Trans. Nucl. Sci.

2009 JINST 4 P04004

[110] A. Biland et. al., *First detection of air shower Cherenkov light by Geigermode-Avalanche Photodiodes*, *Nucl. Instrum. Meth.* **A595** (2008) 165.

[111] I. Braun et al., *First Avalanche-photodiode Camera Test (FACT): A novel camera using G-APDs for the observation of very high-energy-rays with Cherenkov telescopes*, NDIP08, to be published in Nucl. Instrum. Meth. A.

[112] I. Johnson et al., *A Geiger-mode avalanche photodiode array for X-ray photon correlation spectroscopy*, *J. Synchrotron Radiat.* **16** (2009) 105.

2009 JINST 4 P04004